Nano-size effects on optical, structural and phononic properties of VO_2 and WO_3 by ultrasonic-nebulizer spray pyrolysis technique

Bonex Wakufwa Mwakikunga[1]

School of Physics,
University of the Witwatersrand, Johannesburg,
Republic of South Africa.

[1]Supervisor: Elias Sideras- Haddad, (Ph.D), School of Physics, University of the Witwatersrand, Private Bag X3, P O WITS, Johannesburg, Gauteng 2050, Republic of South Africa

A dissertation submitted to the Faculty of Science, University of the Witwatersrand, Johannesburg, South Africa, in fulfillment of the requirements of the Degree of Master of Science.

Abstract

This dissertation presents for the first time the conditions for the synthesis of VO_2 by ultrasonic nebula-spray pyrolysis (UNSP) from a precursor solution of NH_4VO_3+VCl_3 optimized as follows: a carrier gas of argon at a flow rate of 11 liters per minute, a furnace temperature of 400 to 700^{o}C. This work also incorporates thermodynamic variables of T_{pr}-P-V into the equations that relate the mean diameter of droplets, D, to frequency of the exciting ultrasound waves, f, the density of the precursor solution, ρ and the surface tension, σ, previously worked on independently by Lang and Jokanovic. The incorporation results in the diameters of the droplets (and consequently the collected grains) being smaller as p and T_{pr} are increased in a non- linear form. The variable V, however, increases the diameter of the droplets as it is allowed to increase. This study shows the departures many authors find of the theory from experiment but it also shows that the departure does not lie in the equations but rather on post- synthesis and annealing effects. From X-ray diffraction, scanning electron microscopy (SEM) and Raman spectroscopy, this study shows that as furnace temperature is increased the morphology of the sample surfaces for both VO_2 and WO_3 transforms from amorphous to crystalline, from spherical grains to plate-like structures, with grain mean diameter increasing non-linearly in some cases and decreasing non-linearly in other cases confirming previous findings, the latter enjoying the majority vote. In Raman spectra of the as-obtained WO_3, asymmetric broadening of the Raman peaks was observed in some samples and a phonon confinement model was employed in the size distribution prediction. These findings prompted the re- workout of the phonon confinement model. In this dissertation an equation has been derived based on the Faucet-Campbell equation of the PC model. The new equation relates the ratio of neighboring peaks in a material's Raman spectrum to the mean diameter of the grains. The present modification allows the PCM model to predict the grain size beyond the current limiting range of 0 to 100 nm. Analysis of the experimental data using this equation unveils two different

equations- one for particles of size below 100 nm and the other equation for particles with larger that 100 nm. Also this analysis has enabled the present study to evaluate the phonon dispersion relations for WO_3.

In loving memory of my parents
Glynn (1928-2000) and Donnafeg (1935-1968)
and my daughter Ipiana (1994-1998)

Declaration

At the beginning of the year 2004, soon after joining the School of Physics, Faculty of Science, in the University of the Witwatersrand, I was given a challenge of assembling and putting to test some components of equipment (that included an ultrasonic transducer, some glassware, tubing and a furnace) into what has now been called an Ultrasonic Nebulizing Spray Pyrolyzer (UNSP). After successful assembly and following a series of trials and innovations, this materials synthesis technique proved feasible for the first time on materials such as vanadium dioxide from a precursor solution known as ammonium meta- vanadate and, later, the same precursor solution mixed with vanadium chloride. Further trials were done on synthesis of tungsten trioxide from ammonium meta- tungstate hydrate precursor solution. Reports on the success and limitations of this work have already been presented at several local conferences in South Africa. Some articles have also been sent to various journals for a possible consideration for publication.

I declare that this dissertation is my own original, unaided work. It is being submitted for the Degree of Master of Science in the University of the Witwatersrand, Johannesburg, South Africa. This work has not been submitted before for any degree or examination in any other University.

(Signature of candidate)

day of

in the year of our Lord

Acknowledgments

I am deeply indebted and extremely thankful to the Japanese Government and the World Bank for the timely financial support and the whole scholarship through the Joint Japan World Bank Graduate Scholarship Programme (JJWBGSP) in Washington D.C., U.S.A. without which this work would not have been possible at this time.

I would like also to kindly acknowledge the assistance the School of Physics has rendered to me with regard to materials, laboratory space and equipment for research. Special thanks are due to Prof. Barry Cole, the head of the School of Physics for a warm welcome and advice on choice of advisers, Dr. Malik Maaza and Dr. Elias Sideras-Haddad for advice and supervision of my work on vanadium and tungsten oxides, Prof. J Darrell Comins and Mr. Rudolf Erasmus for their continued help in Raman spectroscopy, Dr Giovanni Hearne and Ms Anna Maria Dawe for their help with x-ray diffraction analysis. I am also indebted to the School of Physics at Rand Afrikaans University in agreement with the School of Physics at the University of the Witwatersrand for the UV-Vis IR spectroscopy where optical transitions of my VO_2 materials were unravelled through the assistance of Dr Ouassini Nemoroui. My sincere thanks are also extended to the secretarial, workshop and technical staff in the School for the miscellaneous kindness offers too numerous to detail.

Contents

List of Acronyms

USP Ultrasonic spray pyrolysis

UNSP Ultrasonic nebula spray pyrolysis

SP Spray pyrolysis using pressurized sprayers

FSP Flame spray pyrolysis

LSP Laser spray pyrolysis

RR Resistivity ratio (Ratio of resistivities before and after transition)

HW Hysteresis width (at transition)

SEM Scanning electron microscopy

XRD X- ray diffraction

UV-VIS-IR Ultraviolet- Visible- Infrared

PDF(number) Powder diffraction file (number)

VO_2 Vanadium dioxide

WO_3 Tungsten trioxide

MST Metal to semiconductor transition

List of Symbols

Γ Phonon distribution function.

Λ Ratio of phonon modes 800 cm^{-1} to 700 cm^{-1} as determined from Raman spectroscopy.

Π Ratio of phonon modes 800 cm^{-1} to 700 cm^{-1} as determined from Raman spectroscopy.

Σ Sensor sensitivity function to gases.

α Polarizability function of molecules used in Raman spectral theory.

β A constant in the sensor sensitivity function.

Γ_R Full width at half maximum in Raman spectra

Γ_X Full width at half maximum in X-ray diffraction spectra

D Grain size

q phonon wave number.

$\omega(\mathbf{q})$ dispersion relation for the phonon.

γ A constant in the sensor sensitivity function

η Viscosity of precursor solutions

θ Usually 2θ used in X- ray diffraction

σ Surface tension of precursor solutions

ρ Density of the precursor solution

ω peak Raman shift or Raman frequency

ξ Normal coordinates used in describing the polarizability function.

f frequency of the ultrasonic transducer

M dimension of mass with units in kilogrammes.

L dimension of length with units in metres.

T dimension of time with units in seconds.

M_{pr} Molar mass of precursor solution

M_p Molar mass of the particles after decomposition of the precursor

C_{pr} Concentration of the precursor solution

P gauge pressure in the UNSP system

V volume of the UNSP system

A_g phonon modes allowed in Raman spectroscopy

B_g phonon modes allowed in Raman spectroscopy

$\mathbf{A}_u$ phonon modes allowed in infrared spectroscopy

$\mathbf{B}_u$ phonon modes allowed in infrared spectroscopy

Chapter 1

First synthesis of VO_2 and size-controlled crystallization of WO_3 by ultrasonic spray pyrolysis

In this chapter, a general introduction and objectives of this project are given, a background to the structural, optical, electrical, thermal and other properties of vanadium dioxide (VO_2) and tungsten trioxide (WO_3) are also reviewed. Pertinent terms such as "thermal regulation," "thermal modulation" which are properties of vanadium dioxide (VO_2) (popularly termed "thermo-chromism") are defined. "Sensitivity" and "selectivity" and "electrochromism" which are gas sensing and optical properties of tungsten trioxide (WO_3) are described. A review of the novel synthesis technique 'ultrasonic nebula spray pyrolysis' (UNSP) is also presented.

One of the biggest hindrance to availability of materials for energy conversion, conservation and for environmental applications especially in developing countries has been the cost of producing them. In attempting to bring down the cost of production, the methods of synthesis that are chosen have often compromised on quality of the so- produced materials. There is therefore need to have a method that would embrace both low cost and good quality materials. This is what basic spray pyrolysis would offer.

South Africa, as one of the developing countries, is the leading world supplier of vanadium

ore apart from the fact that it also supplies half of the world gold. This work adds to the pool of knowledge South Africa desperately needs for its building of the capacity and ability to add value to its endowments and mineral resources for the betterment of its people.

The initial objective in this project was to assess the feasibility of UNSP method in the production of multi- phase and difficult- to- produce materials as vanadium dioxide. In this regard there was need to optimize the parameters that are pertinent in the process viz: carrier gas type and its flow rate, furnace temperature, positioning and orientation of the substrate, nature and concentration of the starting solution and pressure in the UNSP system.

Properties of materials tend to drastically change as the sizes of their crystallites and grains are reduced to nano- meter scale where quantum rather than classical physics dominates. A number of misunderstandings on assessment of such novel material properties have been identified such as the conflict between theory and experiment with respect to crystallites sizes estimated by Lang and Jokanovic models (to be introduced in section 1.3) and XRD/SEM experiments and also the conflicts in Raman studies of VO_2. In this study ultrasound waves focused at the surface of a solution were used to produce very small droplets in the micro-meter range which were decomposed to produce powders in the submicro- and nano- meter scales. With experimental facts at hand, it was therefore important to attempt to resolve the above conflicts by observing the deficiencies of the classical physics and the strength of the latter in studying these nanometer sized materials. To this end, phonon confinement models- first proposed by Richter et al (1981)[1] and then modified by by Campbell and Faucet(1986) [2] and further modified by dos Santos et al (1997) [3] (to be discussed in section 2.2 of Chapter 2)- were critically reviewed for the purpose of re-making simpler linear equations relating relative intensity to grain sizes and fitting the so- derived new model to present experimental data.

1.1 Tungsten trioxide (WO_3)

In the last few years a worldwide concern about the necessity for global environmental protection has grown. As a result of this concern, governments have brought in a set of anti-pollution directives. Any attempt to make a serious pollution control requires continuous monitoring

of hazardous gases into the atmosphere. This is a serious problem in developing countries where such resources are scarce. For this purpose, solid- state gas sensors based on semiconductor metal oxides have proven to be promising. These sensors are inexpensive, easy to install and operate. Gases are sensed by their effect on the electrical resistance of the metal oxide semiconductor, resulting from changes in conductivity brought about by combustion reactions occurring within lattice oxygen species on the surface of the film particles [4]

Among several materials that can be used as active layers, tungsten oxide is highly promising. Several studies have shown that WO_3 can be used for the detection of nitrogen oxides (NO and NO_2 and NO_x), carbon monoxide, H_2S, NH_3 and hydrocarbons such as ethanol, benzene and methane[5]-[10]. WO_x electrochromism has been assessed and found to be enhanced when mixed with Au and Al[11], Ti[15], Au, Pd and Pt[18] and mixture with MoO_3[19]. Influence of substrate temperature[20], annealing[12], proton insertion[13], on the properties of WO_x has been reported. Performance of WO_x has been compared with NiO_x on electrochromism[21], with V_2O_5 as sensitive elements for NO detection[22] and with nanopowders of tin and indium oxides as CO and O_2 detectors[23]. In most of these studies, optimisation of selectivity and sensitivity of WO_3 have been the main issues. The worry has been the fact that WO_3 sensitivity reaches its maximum around 350^oC which is a major setback in as far as bringing down the costs of gas sensing is concerned. It has been observed in the current literature that bringing the WO_3 particulate sizes to sub-micrometer levels, or even to nanometer scale, decreases this optimum temperature to regions of 200^oC.

From 0 up to 1200K stoichiometric tungsten trioxide, WO_3, is reported to undergo not less than eight phase transformations in the solid state[24]. Crystallographic information has become available on the WO_3 phases which occur between 900 and -70^{o}C[26]. Below 900^oC, WO_3 is tetragonal, space group P4/nmmm($D^7{}_{4h}$) and transforms at about 740^oC into an orthorhombic modification with space group Pmnb ($D^{16}{}_{2h}$)[27]. Between 17 and 330^oC, WO_3 exhibits monoclinic symmetry, space group $P2_1/n$ ($C^5{}_{2h}$)[28]-[30]. Below 17^oC WO_3, is triclinic, space group P^i ($C^1{}_i$)[31],[32] and transforms at -40^{o}C into another monoclinic phase with space group Pc ($C^2{}_s$) [33],[34]. These WO_3 phases have more or less distorted ReO_3-type crystal structures as illustrated in Figure 1.1[35].

1.1.1 WO_3 applications

An electrochromic material is able to sustain reversible and persistent changes of its optical properties upon the application of a voltage. Integration of such materials in devices makes it possible to regulate transmittance T, reflectance R, absorption A, and emittance E between widely separated extrema. An excellent review of electrochromic devices with WO_3 predominantly applied is given by Granqvist et al [36].

An electrochromic device has a general design as illustrated in Figure 1.2.

1.1.2 The physics of gas sensing

The increasing interest in indoor air quality (IAQ) monitoring is mainly due to the growing incidence of a new class of diseases, identified as building related illnesses (BRI) and sick building syndromes (SBS) arising from the long-term occupancy of confined living spaces that harbour physical, biological and/or chemical contaminants inside the builiding. Typical contaminants are aldehydes, ozone, NO_2, CO_2, CO, particle matter, radon, SO_2, H_2S, Pb, formaldehydes, water vapour and total volatile organic compounds (VOCs). Some of the gases in the above list are obvious greenhouse gases emissions of which the whole world is struggling to cut especially through the recent controversial Kyoto convention/protocol.

The basic property of the sensor material that is employed in sensing the presence of a gas species is usually resistance of that sensor material as a function of sensor surface temperature. The ability to distinguish among the many gases called selectivity of the sensor depends on the resolution of these characteristic temperatures. How high the resistance rises before it falls, or sensitivity, depends on the concentration of the gas that is being sensed. However this calls for another thermodynamic parameter that would be used to analyse these effects, that is, pressure. Sensitivity, Σ is defined as

$$\Sigma = \frac{R_g - R_0}{R_0} \quad or \quad \Sigma = \frac{G_g - G_0}{G_0} \tag{1.1}$$

where R_g, G_g represent sheet resistance and conductance of the sensor when exposed to the gas respectively and R_0, G_0 are the sheet resistance and conductance of the sensor

without the gas. Sheet resistance is measured using a four- point probe technique and the analysis of the value of R_s is done by the Van der Pauw technique. The time dependent non- linear response of a sensor is related to the kinetics of the gas molecules i.e. adsorption, oxidation and desorption on the semiconductor surface and is influenced by the structural and morphological properties of the sensor surface which in turn are dependent on the temperature of the environment. WO_3 is known to have a sensitivity peak around 700K for CO, 525K for NO_2 and 400K for H_2S according to Hoel et al [9] or 623K/673K for CO and 473K for NO_2 according to Guidi et al[6]. Each peak can be fitted with the Gaussian (or any peak function such as the Lorentzian, the Voigtian e.t.c.) of the following nature

$$\Sigma(T) = \Sigma_0 + \frac{Ae^{-2(\frac{T-T_c}{w})^2}}{w\sqrt{\pi/2}} \tag{1.2}$$

where A is the area of the peak, w is the full width at half maximum (FWHM) and T_c is the centre of peak temperature; all these constants are characteristic of the gas being sensed. And if indeed Σ is a function of temperature, T and pressure, p then obtaining values of Σ at varying T, and p would yield a surface in three dimensions whose peaks would be defined by characteristic temperature and pressure values. The relationship between Σ and p has been shown empirically to be directly proportional to p; which means we can write this relationship mathematically as

$$\Sigma(p) = Bp^{\beta} \tag{1.3}$$

where B and β are constants again characteristic of the gas being sensed. Practically, the the two functions of Σ are multiplied to obtain the three dimensional surface of Σ in T and p thus:

$$\Sigma(T,p) = B\Sigma_0 p^{\beta} + \frac{AB}{w\sqrt{\pi/2}} p^{\beta} e^{-2(\frac{T-T_c}{w})^2} \tag{1.4}$$

If there are N gas species to be sensed, then if the sensor is 100% efficient, the number of (Σ(T,p)) peaks in the 3D surface will be N.

1.2 Vanadium dioxide VO_2

Thermo-chromic materials are characterized by a semiconductor-to-metal transition (SMT) occurring from a reversible change in their crystalline structure as a function of the temperature. Thermo-chromism is a term that simply means that the material changes its optical properties due to a varying temperature. Along with a change in optical properties are also electronic transitions evidenced by a change in electrical resistivity. This change has been observed in transition-metal oxides [38],[39] such as Ti_2O_3, Fe_3O_4, Mo_9O_{26} and in several Magneli phases of vanadium oxide, V_nO_{2n-1}. Among them, VO_2 has received the highest attention because of the large reversible change of electric, magnetic and optical properties at temperatures around 70^oC [38]

During the semiconductor-to metal transition, the optical properties of vanadium dioxide are characterized by a sharp decrease in optical transmission in the infrared spectrum. This is coupled with an increasing in its reflectivity. Because of this anomalous behaviour, vanadium dioxide has been presented as an attractive thin film material for electrical or optical switches, optical storage, laser protection, and solar energy control for windows in space satellites. The transition temperature of vanadium dioxide of 70^oC may be decreased by the addition of high-valent transition metals such as niobium, molybdenum or tungsten. Trivalent cations (Cr^{3+} and Al^{3+}) increase the transition temperature. The hysteresis profile associated with the transition depends on the microstructure and crystallinity.

1.2.1 Optical and electronic transitions in VO_2

Since the discovery of the VO_2 semiconductor to metal transition by Morin in 1959[40] VO_2 has been a subject of numerous experimental and theoretical studies. In the first order[40] phase transition of VO_2, the material undergoes a reversible change from a tetragonal rutile structure phase, space group $P42_{mnm}$ with typical lattice constants a = 4.5546 and c = 2.8514 $\mathring{A}$, at higher temperature to a monoclinic structure, space group $C2_m$ with lattice constants a=12.09 b=3.702, 6.433 $\mathring{A}$ and 106.6^o, below the phase transition. The typical structures are represented in Figures 1.3 to 1.6. These structural characteristics led Good-

enough[37] to propose a model of the electronic structure based on molecular field theory that has accounted for some properties of VO_2 metallic and semiconducting phases[43]. This model has subsequently undergone further improvements by incorporating electron-electron correlations[44] and electron-phonon interactions.

1.2.2 VO_2 applications

Among the transition metal oxides exhibiting semiconductor to metal structural phase transition, vanadium dioxide is the most spectacular example. This is due to the large change of its physical properties such as resistivity, transmittance, and reflectance during this phase transition. This has led to, vanadium dioxide being studied, not only from the fundamental point of view, but also for potential applications in electronics, optics or opto-electronics This interest is especially generated by large changes of resistivity, optical transmission, and reflection in the infrared. These changes are associated with a hysteresis loop when the material is heated and cooled around the temperature of phase transition.

Because of the ability to change the transition temperature by doping, Lee et al [45] and more recently P. Jin et al. [46], suggested that tungsten doped vanadium dioxide can be used in energy efficient-windows. These smart windows or electrochromic displays find special applications in the architectural, automotive and aerospace sectors [47]. Roach [48] pointed out that, due to the changes in reflectivity during the phase transition, VO_2 films can be used as a kind of optical disc medium and demonstrate holographic storage.

Bit recording on VO_2 films using a near-infrared laser was demonstrated [49]; stability during long-term storage and over 10^8 time-cycles of write and erase were achieved without degradation. Switching time of about 30 ns and writing energy of the order of a few mJ/cm^2 were reported[50]. Bit density has been estimated to be 350 bits/mm. Such low threshold recording energy and erase-re-writability encourage the use of VO_2 films as a recording medium[51].

More recently, the use of VO_2 thin films was suggested in ultrafast optical switching devices. The high-temperature metallic state attained in 5ps by using femto- second laser excitation at 780 nm was reported[53].

In summary, vanadium dioxide is an interesting candidate for modern applications of active thin films in optical or electric[54] switches. The ultrasonic spray pyrolysis process is an attractive approach for preparing these films and nano- powders. The applicability of this kind of coatings needs more work on device feasibility, reproducibility and scale-up processes.

1.3 Ultrasonic nebula-spray pyrolysis process

Although a lot of achievements and progress have been made during the past few decades, it has also been found that both bulk and thin-film single-crystal VO_2 are difficult to grow, which frustrates attempts to achieve a deep understanding of the mechanism of the semiconductor-metal transition (SMT) and related phenomena. In addition, some attempts [9],[10] have been made to reduce the phase transition temperature, T_t by incorporating dopants, but T_t can only be decreased at the expense of a degradation of the film properties; the explanation of the release of stress is far from satisfactory, and much more insight from further study is needed, which relies on the growth of a high-quality thin films of VO_2. Much effort has been devoted to the preparation of high-quality VO_2 film by different preparation methods [11]-[16]. It has been reported that highly oriented VO_2 thin film prepared by pulsed-laser ablation [17],[12] exhibits good properties with a high ratio of the resistivity (RR) before the phase transformation to that after transformation and a small hysteresis width (HW) (2 x10^4 and 2^{o}C respectively).

For developing countries, this difficulty in growth of VO_2 is compounded with the dire need for a way of mass producing the VO_2 based materials. The easiest route to mass production is spray pyrolysis. For more efficient and purer products, it is desirable to produce much finer droplets in the spray than are produced by traditional pressurized sprayers. Excitation of the precursor solution with ultrasonic waves is seen to be the next state- of- the- art technique.

Ultrasonic spray pyrolysis (USP) involves material deposition by exciting precursor solutions with surface focused ultrasound waves thereby creating much finer precursor droplets than have been achieved hitherto by other traditional pressurized nebulizers. A schematic diagram of the UNSP system is given in Figure 1.7.

Ultrasonic vibrations set up standing waves on the surface of a liquid such that at a critical environment the surface erupts into fine droplets whose diameters D are proportional to the ultrasonic transducer frequency f, the liquid density ρ, its surface tension, σ. This relationship is studied using dimensional analysis by considering the dimensions of f as $[\mathrm{T}^{-1}]$, ρ as $[\mathrm{ML}^{-3}]$ and σ as $[\mathrm{MT}^{-2}]$. Mathematically, this assertion is presented thus:

$$D \propto f^x \rho^y \sigma^z \tag{1.5}$$

That is

$$D = k f^x \rho^y \sigma^z \tag{1.6}$$

Where k is a dimensionless constant and x, y, z are coefficients to be worked out. Expressing Equation 1.6 in terms of the dimensions of the variables involved we have

$$[L] = [T^{-1}]^x [ML^{-3}]^y [MT^{-2}]^z \tag{1.7}$$

where upon balancing of the powers on the LHS with those on the RHS we get

$$y = -\frac{1}{3} \quad x = -\frac{2}{3} \quad z = \frac{1}{3} \tag{1.8}$$

which means that

$$D = k(\frac{\sigma}{\rho f^2})^{\frac{1}{3}} \tag{1.9}$$

As early as 1962 the value of k was empirically determined to be $0.68\pi^{1/3}$ by Lang [61] and in 1996 Jokanovic et al derived it to be simply $\pi^{1/3}$ [62]. From the knowledge of the approximate diameters of the droplets, we can estimate the expected sizes of the as- deposited nano- particles using the derived expression from the above Equation 1.9 given respectively as

$$d_{pL} = D_L \left(\frac{c_{pr} M_p}{\rho_p M_{pr}} \right)^{\frac{1}{3}} \tag{1.10}$$

$$d_{pJ} = D_J \left(\frac{c_{pr} M_p}{\rho_p M_{pr}} \right)^{\frac{1}{3}} \tag{1.11}$$

where c_{pr} is the precursor concentration, M_p is the molar mass for the as-deposited particles, M_{pr} is the molar mass for the precursor, ρ_p is the density of the as- deposited nanoparticles and D_L and D_J are Lang and Jokanovic droplet diameters respectively.

These expected particles sizes can also be estimated from X- ray diffraction (XRD) peaks as illustrated by Guinneton et al (2000)[6] results of which can be compared with those obtained using the previous equations. This is normally done by determining the full width at half maximum (FWHM) of the VO_2 and WO_3 strongest peaks emanating from VO_2 and WO_3 crystal faces with Miller indices (011) and (100) respectively the distributions of which are centred around $2\theta = 27.783^o$ and 23.986^o respectively in the VO_2 and WO_3 XRD spectra respectively and using the Scherrer formula given as

$$d = \frac{0.9\lambda}{\Delta\left(2\theta\right).cos\theta} \tag{1.12}$$

where $\Delta(2\theta)$ is known as broadening due to size effect which at low Bragg angles is calculated thus

$$(\Delta 2\theta)^2 = (FWHM)^2 - \varpi^2 \tag{1.13}$$

where ϖ is the standard FWHM obtained from the standard VO_2 and WO_3 samples which in this case were 0.089^o and 0.092^o respectively.

Ultrasonic Spray Pyrolysis like the traditional spray pyrolysis has attractive features of simplicity, economic viability, high deposition rate, possibility of coating over large areas and continuous operation. But, unlike other commonly known atomizers such as pressure nozzles, it has, as cited by Cho et al (1997) [63], the advantages of "high purity, chemical purity and stoichiometry" and allows a narrow distribution of particle sizes. In particular, as specified

by Chang et al (2000)[64], a large proportion of droplets below 20 μm are typically produced with a low in- flight speed. This prevents droplets from being removed from the gas phase by impact onto walls of the reactor. The major disadvantages being potential for hollow structure or fractured particles [63] and that the droplet production rate is typically low and highly dependent on the throughput of the nebulizer[64].

USP is reported by Ivanov-Schitz et al 1989[65] to have been employed by Langlet et al[66] as early as 1989 in the deposition of Y-Ba-Cu-O superconducting films, in 1990 by Setoguchi et al[67] in the deposition of calcia films, by Saito et al[68] and Hong et al [69] in 1994 for production of $Na_4Zr_2Si_3O_{12}$ and $NaZr_2P_3O_{12}$ powders respectively. Similarly Kamiya et al [70], Furusaki et al[71], Huang CS et al[72] and Matsuzaki et al [73] and Huang H et al [74] employed USP in the development of ceramics, $LaCrO_3$- based oxide films, $Pb(Zr,Ti)O_3$ thin films, yttria films and silicon doped tin oxide films respectively. Interestingly, nanopowders of tetragonal doped and undoped ZrO_2 are reported by Ivanov-Schitz et al[65] to have been produced by USP by Djurado et al[75] in 1998. Although Raju, Aiyer and Rao[76] in 1995 claim the USP method was developed in their laboratory, they do acknowledge the prior report by Langlet and Joubert[78] in 1993 on the Chemistry of Advanced Materials. It is likely that Raju et al[77] modified the Langlet procedure to suit their objectives of applying the method to pyrolysis of $PbTiO_3$, $(Pb,La)TiO_3$ and $Pb(Zr,Ti)O_3$ in 1995 [78] and also as reported by Murugavel et al[79] in 1997 who used USP in metal- organic precursors to produce TiO_2, ZrO_2 and PZT.

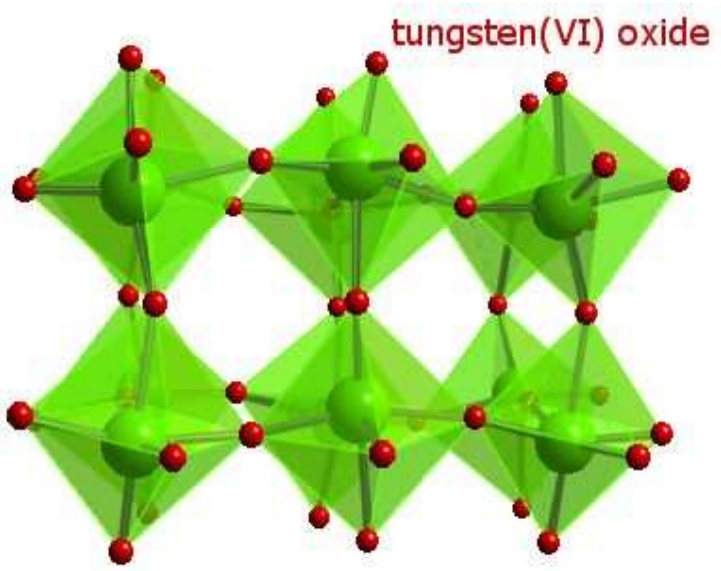

(a)

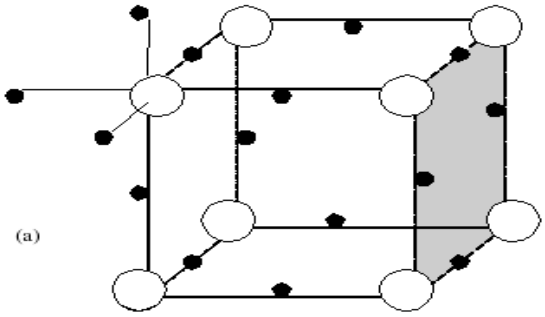

(b)

Figure 1.1: The edge-sharing rhenium trioxide (ReO_3) structure (a) from which WO_3 adopts its own distorted variant structure (b)

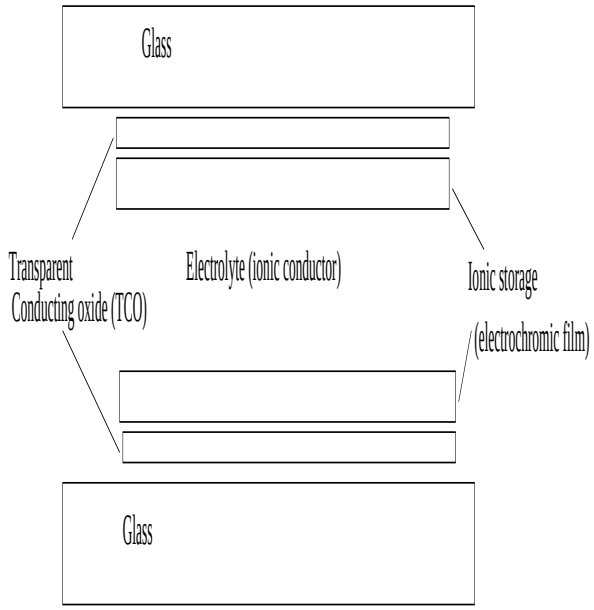

Figure 1.2: A general design of an electrochromic device

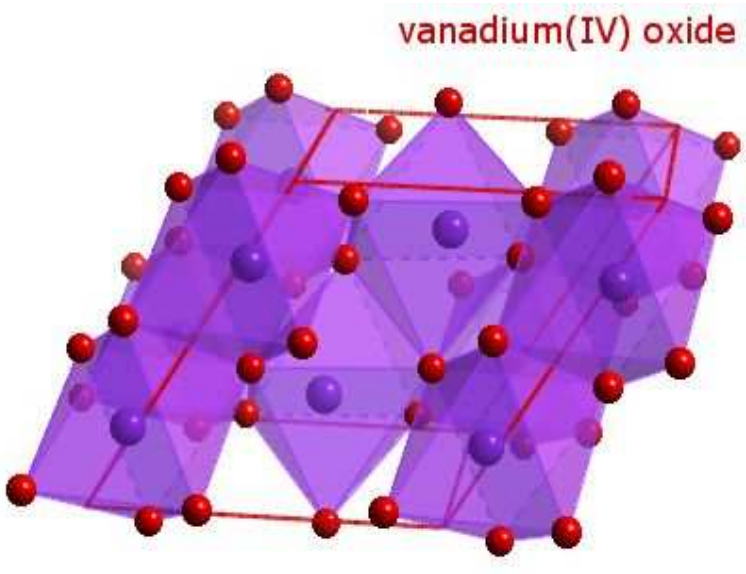

Figure 1.3: This is the top view of the VO_2 rutile and monoclinic structure

Figure 1.4: Side view of the VO_2 rutile and monoclinic structures

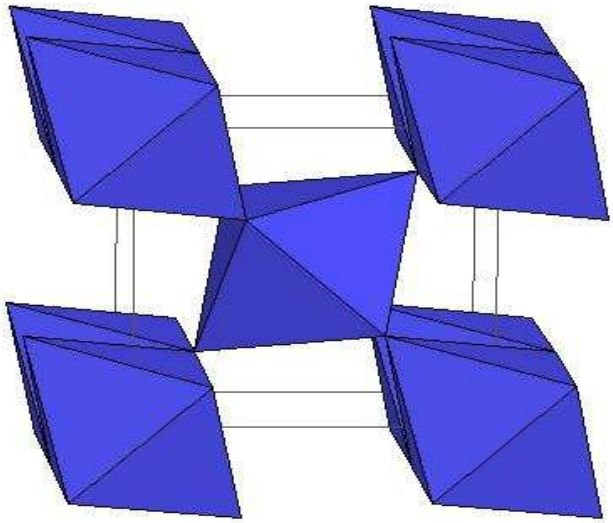

Figure 1.5: Typical TiO_2 rutile structure which VO_2 adopts at high temperatures

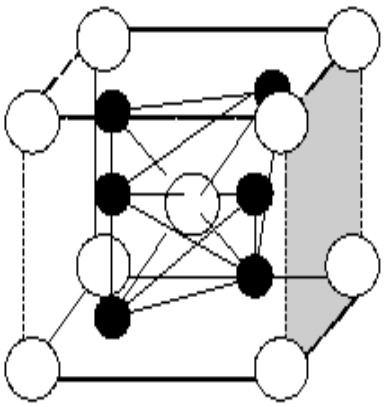

Figure 1.6: Atomic representation of the VO_2 rutile unit cell

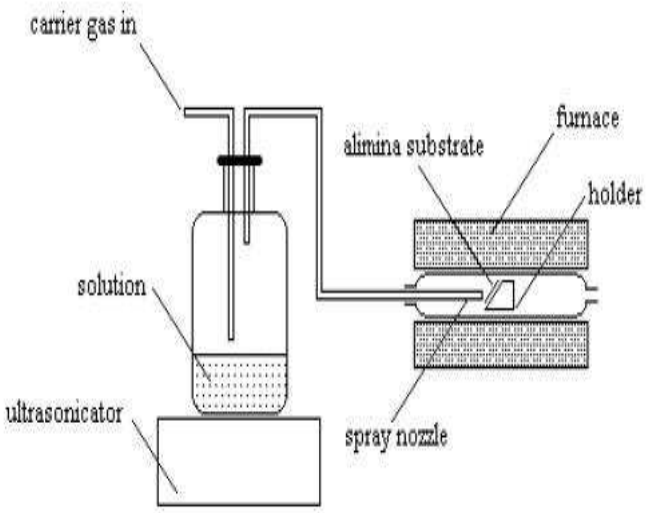

Figure 1.7: A schematic representation of the ultrasonic nebulizing spray pyrolysis technique. A more elaborate presentation with photographs of the experimental site is given in Chapter 3

Chapter 2

Droplet-to-solid particle transformation, the phonon confinement model and the presently proposed parallel models

In this chapter a review of over eighty publications on materials synthesis using different forms of spray pyrolysis and their grain diameter determination results are reviewed. Especially unveiled is the conflict that most authors find between calculated grain sizes using Jokanovic or Lang equations as presented in Chapter 1 and those experimentally measured using either scanning electron microscopy or X- ray diffraction. Proposed in this treatise are some answers to this conflicts by introducing the following pertinent factors:

1. The first factor is the temperature of the precursor solution as one parameter during the droplet production process that all authors have hitherto not considered. This parameter critically affects the pertinent parameters of density and surface tension in the Lang and Jokanovic equations.

2. A second factor is the gauge pressure of the USNP system with reference to the atmospheric pressure.

3. The third and most interesting factor is the volume of the vessel that is housing the generated droplets

4. A fourth factor is the temperature of deposition of the particles that, sometimes, is referred to as calcination or annealing temperature.

These factors have enabled the present study to generate yet another model that is able to explain a number of findings that have hitherto lacked physical and scientific explanation as will be shown in the next sections of this chapter.

2.1 Proposed refinement of the Lang-Jokanovic droplet size model

As already introduced in the previous chapter, the first explanation for the phonomenon of droplet generation from liquids by ultrasound waves was given by Lang (1962) [63] and his semi-empirical equation is given as [4]-[18]

$$D = 0.68\,(\pi)^{1/3}\,(\frac{\sigma}{\rho f^2})^{\frac{1}{3}} \tag{2.1}$$

In 1996, Jokanovic et al (1996) [64], formulated another parallel equation based on a partial differential equation of motion of the droplet in an ultrasonic mechanical wave field and managed to show that droplet diameters from ultrasonic spray could be calculated from the following equation:

$$D = (\pi)^{1/3}\,(\frac{\sigma}{\rho f^2})^{\frac{1}{3}} \tag{2.2}$$

Both of the above models assumed that the thermodynamic properties of the precursor liquid in the USP system (such as pressure, system volume and system pressure) are negligible. However, in a real experimental situation, it is observed that every ultrasonic nebulizer increases the temperature of the precursor solution. Inclusion of a temperature dependent surface tension and density in the above models would improve the agreement between theory

and experiment. Also, the pressure (p) in the USP system and shape and size (V) of the USP system are considered pertinent factor in the ensuing model. The droplet diameter can then be expressed as

$$D\left(p, V, T_{pr}\right) = k\left(\frac{\sigma(T)}{\rho(p, V, T_{pr}) f^2}\right)^{\frac{1}{3}} \tag{2.3}$$

and the deviation of the droplet diameter from the expected value due to change in surface tension and density which in turn are due to changes in precursor solution temperature and UNSP system pressure can be found by taking a first derivative of Equation 2.3 above and this can be shown to take the form of

$$\frac{\Delta D}{D} = \frac{1}{3}\left(\frac{\Delta\sigma}{\sigma} - \frac{\Delta\rho}{\rho}\right) \tag{2.4}$$

Also, in a case where the ultrasound-focused surface level is not constant with time, the out-of-focus effects of bulk precursor properties such as viscosity may also need to be included in the models. (In this case, running through the dimensional analysis for the case of D being dependent on viscosity, η rather than density, ρ, the following expression for d is obtained:

$$D = k'\left(\frac{\sigma}{\eta f^2}\right)^{\frac{1}{3}} \tag{2.5}$$

and similarly

$$\frac{\Delta D}{D} = \frac{1}{3}\left(\frac{\Delta\sigma}{\sigma} - \frac{\Delta\eta}{\eta}\right) \tag{2.6}$$

Equations 2.4 and 2.6 show similar characteristics. This means that the density of the starting liquid and its viscosity has similar error effects on droplet diameter. Since many researchers have used density rather than viscosity, the present discussion opts to use density throughout this treatise. In addition, the effects of substrate temperature and annealing temperature and duration of annealing, all need to be inserted in the models when estimating the size of the so-obtained grains on a substrate.

From thermodynamics it is possible to deduce that surface tension reduces upon an increase in temperature of a liquid. The relation between σ and T_{pr} from a rigorous analysis is given as

$$\sigma = H + T_{pr}\frac{d\sigma}{dT_{pr}} \tag{2.7}$$

where H is the energy required to increase the area of the surface of the liquid in contact with air by unit area and T_{pr} is the temperature of the precursor solution in kelvin units. It should be noted that the energy H is always positive and it follows from the fact that σ decreases as T_{pr} increases that the derivative is always negative. For many liquids H is about +50 $mJ.m^{-2}$ and the derivative about -0.1 $mJm^{-2}K^{-1}$.

Density ρ can be written as a function of temperature from van der Waals real gas equation (in present study, the real gases are droplets or vapours)

$$\left[p + \frac{a\rho^2}{M_{pr}^2}\right]\left[V - \frac{\rho V b}{M_{pr}}\right] = \frac{\rho V R T}{M_{pr}} \tag{2.8}$$

where a and b are the usual constants that depend on the real gas which for this case are very close to those of water vapour (a = 0.5507 Jm^3mol^{-2} b = 3.04 x 10^{-5} m^3mol^{-1}), M_{pr} is the molar weight of the precursor solution material, p is the pressure in the chamber and V is the volume of the chamber, R is the universal gas constant (0.082025 atm $mol^{-1}K^{-1}$). This has been accomplished by substituting in the original van der Waal's equation the following facts:

$$n = \frac{m}{M_{pr}} = \frac{\rho V}{M_{pr}} \tag{2.9}$$

where n is the number of moles

From Equation 2.8 one gets three solutions of density ρ two of which have imaginary parts in them. The one solution that is completely real is given as:

$$\rho\left(p, T_{pr}\right) = \frac{M_{pr}}{3b} + \frac{0.42\Omega_1\left(p, T_{pr}\right)}{ab\Omega_2\left(p, T_{pr}\right)} + \frac{0.264\Omega_2\left(p, T_{pr}\right)}{ab} \tag{2.10}$$

where

$$\Omega_1 (p, T_{pr}) = 3abM_{pr}^2 (bp + RT) - a^2 bM_{pr}^2 \tag{2.11}$$

and

$$\Omega_2 (p, T_{pr}) = (\chi + B)^{1/3} \tag{2.12}$$

and

$$\chi = 2a^3 M_{pr}^3 + 18a^2 b^2 M_{pr}^3 p - 9a^2 bM_{pr}^3 RT \tag{2.13}$$

$$B = \sqrt{(\chi + 4\Omega_1 (p, T_{pr})]} \tag{2.14}$$

The positive ρ solution is chosen so that the d is not imaginary. By substituting 2.7 and 2.10 into 1.9 in Chapter 1 one gets

$$D (p, T_{pr}) = k \left[\frac{H - CT}{f^2 \left(\frac{M}{3b} + \frac{0.42\Omega_1 (p, T_{pr})}{ab\Omega_2 (p, T_{pr})} + \frac{0.264\Omega_2 (p, T_{pr})}{ab} \right)} \right]^{\frac{1}{3}} \tag{2.15}$$

After substituting the values of the constants a, b, M_{pr}, R, H and C, as presented in Table 2.1, the droplet diameter relation reduces to

$$D (p, T_{pr}) = k \left[\frac{0.05 - 0.0001 T_{pr}}{1.1 \times 10^5 M_{pr} + 1.6 \times 10^5 \left(\sqrt{M_{pr}^6 F^2 + 4G^3} + M_{pr}^3 F \right)^{1/3} + \frac{M_{pr}^2 (7.6 \times 10^3 - 3.83 \times 10^{-5} - 10.33 T_{pr})}{\left(\sqrt{M_{pr}^6 F^2 + 4G^3} + M_{pr}^3 F \right)^{1/3}}} \right]^{\frac{1}{3}} \tag{2.16}$$

where

$$F = 3.3 \times 10^{-1} + 5.0 \times 10^{-9} p - 6.8 \times 10^{-4} T_{pr} \tag{2.17}$$

and

$$G = 4.1 \times 10^{-4} T_{pr} - 3.0 \times 10^{-1} + 1.5 \times 10^{-9} p \tag{2.18}$$

When calculations are done for temperatures between room temperature and the boiling temperature of water (100°C) and for pressures around atmospheric pressure, then F and G tend to be negligibly small and the droplet diameter expression finally reduces to

$$D\left(p, T_{pr}\right) = k\left[\frac{0.05 - 0.0001T_{pr}}{1.1 \times 10^{5} M_{pr} + \frac{M_{pr}^{2}(7.6\times10^{3} - 3.83\times10^{-5} - 10.33T_{pr})}{\left(\sqrt{M_{pr}^{6}F^{2}+4G^{3}}+M_{pr}^{3}F\right)^{1/3}}}\right]^{1/3} \tag{2.19}$$

The advantage of this presently proposed model is that it does not require the investigator to look up values of surface tension and density for every precursor solution. Indeed these values are usually not available in literature. These difficult-to-measure constants have been replaced by constants that are widely available in handbooks and thermodynamics textbooks. The present model however adds sophistication to the UNSP set up in that the system pressure, volume and the precursor temperature have to be monitored during experiment by an addition instrumentation. This is a good practice for accuracy's sake.

Table 2.1: Table of constants for the present proposed model

Symbol	NH_4VO_3 precursor for VO_2	$(NH_4)_6W_7O_{24}.6H_2O$ precursor for WO_3	Units
M_{pr}	116.98	1887.19	a.m.u
Gas constant,R	8.2	8.2	$Jmol^{-1}K^{-1}$
a	0.5507	0.5507	Jm^3mol^{-2}
b	3.04×10^{-5}	3.04×10^{-5}	m^3mol^{-1}
C_{pr}	10	6.7	kg m^{-3}
M_p	82.941	231.84	a.m.u.
ρ_p	4330	7200	kg m^{-3}

2.1.1 Droplet diameter as a function of the precursor temperature

The current model has been analyzed in order to get a picture on the effects of p and T_{pr} on the droplet diameter D. At constant pressure (atmospheric) the D(T_{pr}) relation reveals a profile as illustrated in the two-dimensional plots of the D in as a function of T_{pr} in Figure 2.1.

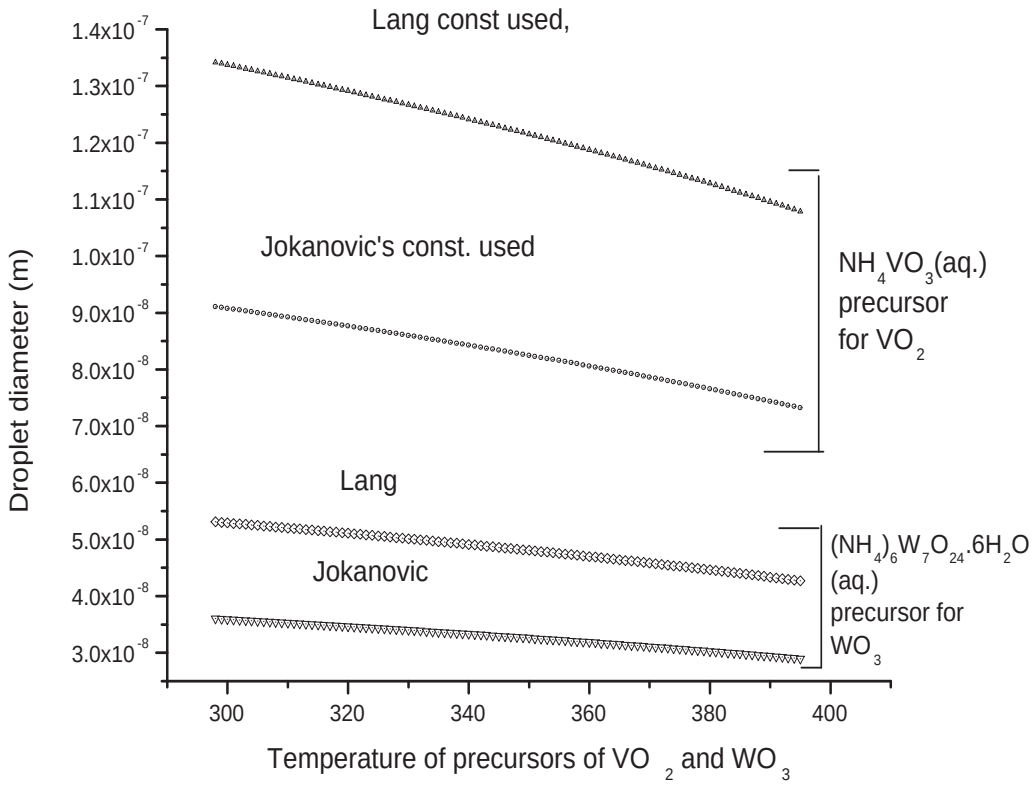

Figure 2.1: A plot of the droplet diameter D versus precursor temperature at a constant UNSP system volume of 3 liters and a constant atmospheric pressure

The plot in Figure 2.1 reveals the fact that, due to the reduction in surface tension as the precursor temperature is raised, the droplet diameter also tends to decrease. This is true for both precursors considered in this study. Droplet diameters calculated using the Lang's constant gives smaller values than using Jokanovic's constant as expected. It can also be seen from this graph that the WO_3 precursor solution produces smaller droplets than those of VO_2.

2.1.2 Droplet diameter as a function of the USP system pressure

The current model was used to show droplet size profile at constant (room) temperature at varying pressure and a typical plot is as presented in Figure 2.2.

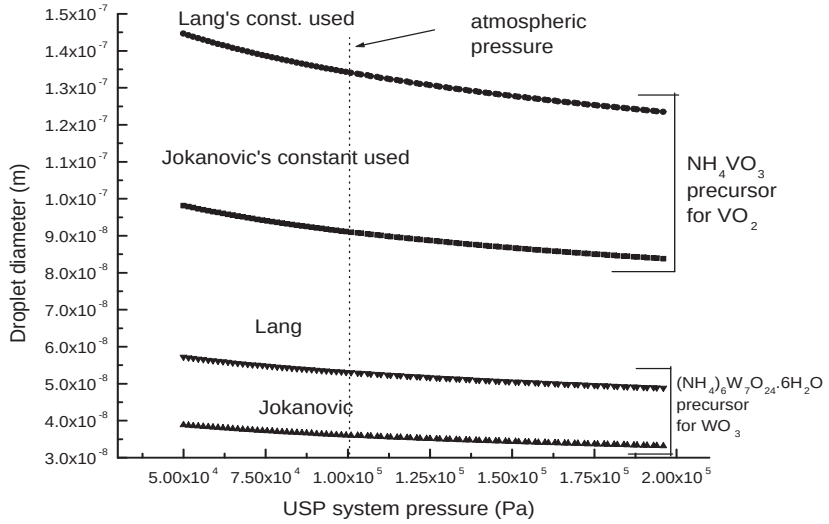

Figure 2.2: A plot of the droplet diameter against USP system pressure around atmospheric pressure at a constant UNSP system volume of 3 liters

.

Again, one sees that increasing pressure tends to stress the droplets and smaller droplet diameters are obtained.

2.1.3 Droplet diameter as a function of USP system volume

This is not clearly apparent from the Van der Waal's equation inclusion into this model since volume cancels out. This only uncovers inherent weaknesses in the van der Waal's equation of state bearing in mind the experimentally and inexplicable effect volume occupied has on the size of the droplets as will be mentioned later on in this dissertation.

In this study, the Bernoulli's theorem of conservation of energy of fluid flow in channels of varying cross-sectional area was considered useful in deriving the relationship between droplet size and the volume it occupies. Starting from the fact that when all fluid parameters of pressure, density and velocity at different positions in the flow system are not constant, Bernoulli's theorem states that

$$p + \frac{1}{2}\rho v^2 + \rho g y = constant \tag{2.20}$$

Operation of the Chain rule to these varying parameters, following the ρ=m V substitution, yields

$$dp + \left[\frac{1}{2}mv^2 + mgy\right] dV + \rho v dv + g\rho dy = 0 \tag{2.21}$$

And the assumption that droplet size change with velocity is not large and more or less constant in a typical materials deposition process, then dv is almost equal to zero and the expression reduces to

$$dp = -EdV - g\rho dy \tag{2.22}$$

where E is the total energy of the droplet. If droplet diameter is introduced into this relation, it is possible to write

$$\frac{dD}{dp} = -\frac{dD}{EdV + g\rho dy} \tag{2.23}$$

which indicates that either at a constant position y but varying volume V

$$\frac{dD}{dp} \propto -\frac{dD}{EdV} \tag{2.24}$$

or for a fixed volume of the system V but varying position y

$$\frac{dD}{dp} \propto -\frac{1}{g\rho}\frac{dD}{dy} \tag{2.25}$$

A plot of droplet diameter versus USP system volume in line the above discussion is given is Figure 2.3.

The plot reveals how critical the volume of the USP system is in influencing the size of the droplets. For reasons not yet understood, the larger the volume that droplets occupy in the USP system the larger the droplets formed. It can also be seen from these analyses that

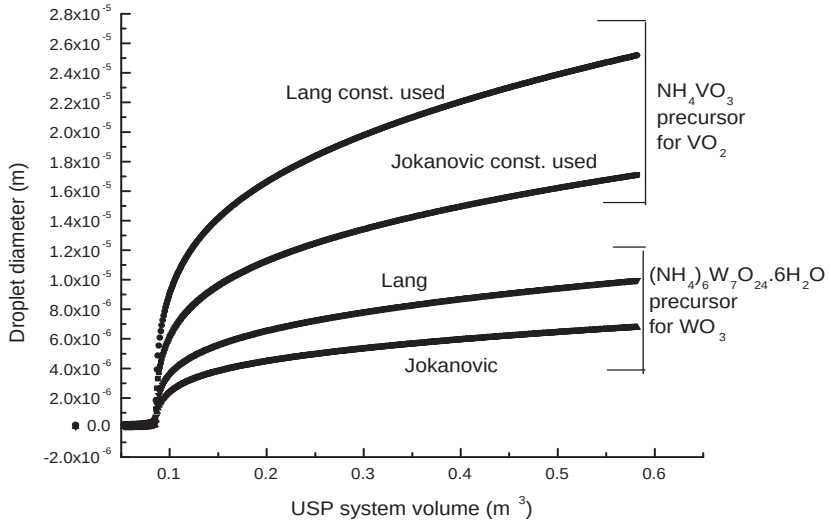

Figure 2.3: A plot of the droplet diameter as a function of the USP system volume at a constant UNSP system pressure of 1 atm (100kPa) and a constant room temperature of 298K

precursor materials with large molecular masses tend to form smaller grains in line with Equations 1.10 and 1.11. The results chapter in Chapter 4 has some recent experimental findings that confirm the theory discussed in this section.

2.2 Phonon confinement model for Raman intensities from *nano*crystals and the present proposed extension of this model to *micro*crystals

Phonon confinement models were developed in the 1980's to account for the experimental observations for *micro*-crystalline Si films by Richter et al (1981)[1]. In fact, during this time, these authors named this model "SPATIAL CORRELATION MODEL"[88]. The development of these models came about after experimental observations that when materials had some disorders, the characteristic peaks in a Raman spectrum of such materials showed shifts in peaks either blue-shift (to higher frequencies) or red-shift. In addition peaks were

seen to broaden in an asymmetrical manner especially toward the lower frequency side of the peak. This led Richter et al to suggest the following expression for intensity as a function of the Raman frequency:

$$I(\omega) = \int_{-\infty}^{\infty} \frac{d^3q \ |C(0,q)|^2}{[\omega - \omega(q)]^2 + \left(\frac{\Gamma_0}{2}\right)^2} \tag{2.26}$$

where $|C(0,q)|^2$ are the Fourier coefficients and q if the wave number or wave vector and a is the lattice constant. ω(q) is the phonon dispersion equation and Γ_0 is the natural (or bulk) width (FWHM) of the Raman peak.

Faucet and Campbell (1986) tried several Fourier related function including the Gaussian, the sine function, the Lorentzian and other peak functions in order to fit some Raman spectra of disorder SiO_2. From this study, they found that the Gaussian gave the best fit. Since then, a number of author have tried several functions but the Gaussian remain the ubiquitous one.

2.2.1 Phonon confinement model

For a perfect crystal, conservation of momentum requires that, in first order Raman scattering, only optic phonons near the centre of the Brillouin zone (q=0) are involved and contribute to the observed Raman peak. In disordered materials or spatially confined systems due to lack of long range order, the q vector selection rule does not apply and the range of q vectors having their wave vectors non-zero are also accessible. As a result, a contribution from $\mathbf{q} \neq 0$ phonons determined by the dispersion relation $\omega(\mathbf{q})$ is allowed.[92] This is what is believe to account for the asymmetric broadening of the Raman peaks in nanometric materials.

If one considers two Raman spectra A and B of a material in bulk form (A) and in nanocrystal form (B) in Figure 2.4.

It has been widely observed that when nanocrystal diameters get into the region of less than 100 nm the Raman peaks emanating from such NCs are asymmetrically broadened. This has been explained as being due to the spatial confinement of phonons in a finite volume (of the order of a few angstroms[2]). In this case, this phonon confinement is expected to relax the wave vector selection rules and cause modifications in the bulk Raman peaks, such as peak

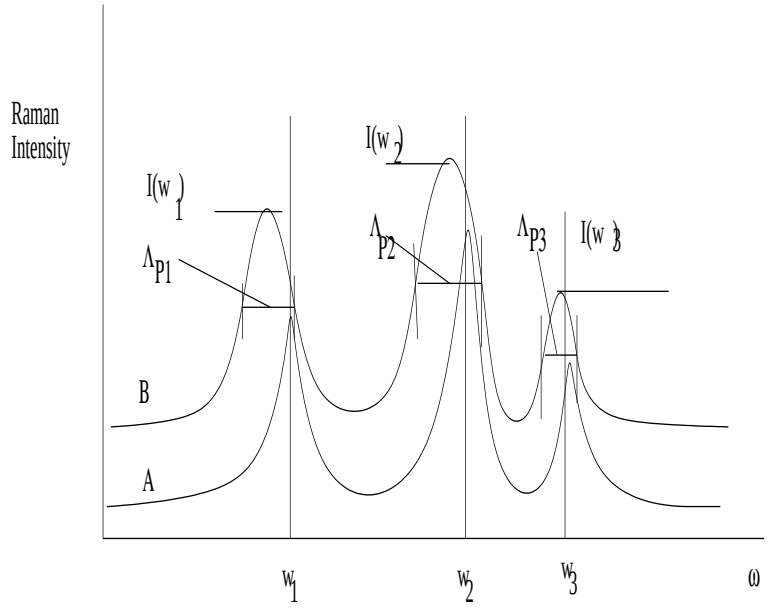

Figure 2.4: An example of the effect of size of crystals on the Raman spectra- curve A: bulk and curve B: nanocrystal

frequency shifting, peak broadening, and emergence in peak asymmetry[3]. An expression of Raman intensity as a function of phonon dispersion for a given peak frequency was first derived and reported by Faucet and Campbell in 1986 [2] and generally given as

$$I(\omega) = \int_{-\infty}^{\infty} \frac{d^3q \;\; e^{-\left(\frac{q^2 d^2}{4\pi^2}\right)}}{\left[\omega - \omega(q)\right]^2 + \left(\frac{\Gamma_0}{2}\right)^2} \tag{2.27}$$

where q is the wave number and ω is the frequency of a particular phonon, ω(q) is the dispersion relation for the material, d is the grain size and Γ_0 is the natural line width for the particular material. One complication has been the limits of the integral in Equation 2.27; some author take the integral from 0 to ∞, others from -∞ to +∞ while in some cases it is evaluated from 0 to the first Brillouin zone (2π/a) where a is the lattice constant. In all cases the integral has often been evaluated numerically.

2.2.2 The present modification to the phonon confinement model

It has been reported by Kubo et al[87] that the ratio of the integrated Raman scattering intensities of the W=O band to that of the O-W-O band in the region of 600- 900 cm^{-1} can be employed as the measure of the relative cluster size. The quantity of W=O terminal bonds around the cluster is inversely proportional to the cluster size. Kubo et al made this assertion purely from empirical evidence of the temperature dependence of the cluster size in WO_3. Grain size direct correlation to annealing and/or deposition temperature is a well documented fact and this has also been shown in this work (especially on page 86 in Figure 4.12) that grain size and deposition temperature are directly related.

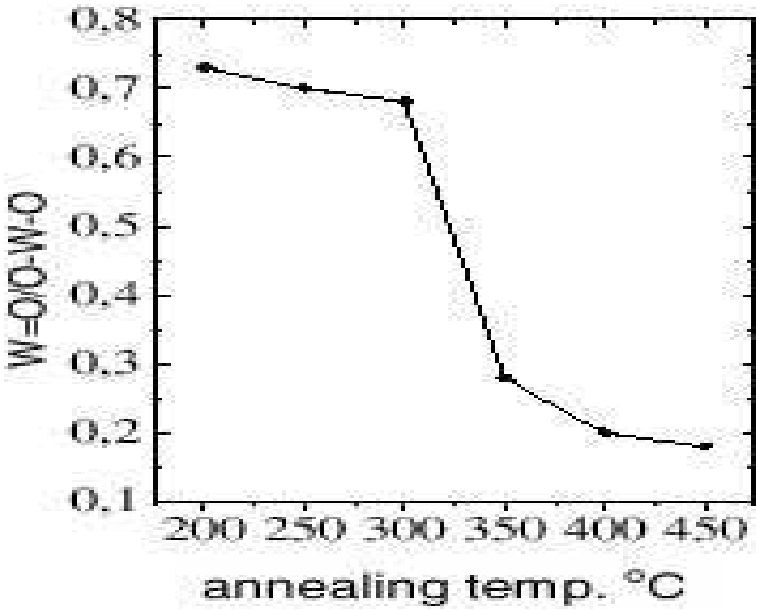

Figure 2.5: Ratio of intensities of peak 800 to 960 cm^{-1} found by Kubo et al and report by Bittencourt et al (Ref. 1)

Having found similar results to those of Kubo et al which are as illustrated in Figure 2.5, in this dissertation, an attempt has been made to quantify the fact that the ratio of Raman peak intensity of neighboring peaks can be correlated to the mean diameter of the grains even outside the restricted minimum of 100 nm. This ratio of neighboring peak intensities is first represented as a ratio of the integral in Equation 2.27 as follows:

$$\frac{I(\omega_1)}{I(\omega_2)} =_1 \Pi_2 = \frac{\int_{-\infty}^{\infty} \frac{d^3q \;\; e^{-\left(\frac{q^2d^2}{4\pi^2}\right)}}{[\omega_1-\omega(q)]^2+\left(\frac{\Gamma_0}{2}\right)^2}}{\int_{-\infty}^{\infty} \frac{d^3q \;\; e^{-\left(\frac{q^2d^2}{4\pi^2}\right)}}{[\omega_2-\omega(q)]^2+\left(\frac{\Gamma_0}{2}\right)^2}} \tag{2.28}$$

The task is first to substitute a suitable phonon dispersion relation ω(q) to the system one is studying. Different transition metal oxides have different ω(q) relation [81] $\rightharpoonup$ [88] as tabulated below:

$$\omega(q) = \begin{cases} k + hcos(\pi q), & Si(NCs) \\ 143.5cm^{-1} + (164cm^{-1})sin^2\left(\frac{\pi q}{1.51779}\right), & TiO_2 \\ 815.6 - 72q^2, & Zr_5TiO_4 \\ 143cm^{-1} + 28(1 - cos(aq)), & TiO_2 \\ 143cm^{-1} + 102(1 - cos(aq)), & TiO_2 \\ \omega_1 = 69 - 13.52q + 1042q^2 - 4264q^3 + 6863q^4, & c - Bi \\ \omega_2 = 96.8 - 18q - 99.1q^2 + 120q^3 - 40.4q^4, & c - Bi \\ \omega^2(q) = 4.7 \times 10^4 cm^{-2} + \left[(4.7 \times 10^4 cm^{-2})^2 - (2.2 \times 10^4 cm^{-3})sin^2\frac{aq}{2}\right]^{1/2}, & SiO2/CdS \end{cases} \tag{2.29}$$

The second problem is to evaluate each integral in Equation 2.28 and obtain a compact relation between $_1\Pi_2$ and grain size, d. To reduce further clumsiness, it is easier to evaluate one integral at a time and then proceed to taking the ratio of the proceeds. The numerator integral in Equation 2.28 can be rearranged thus:

$$I(\omega_1) = \Gamma_0 \int_0^{\infty} e^{-\frac{q^2d^2}{4\pi^2}} \left[1 + \frac{4(\omega_1 - \omega(q))^2}{\Gamma_0^2}\right]^{-1} d^3q \tag{2.30}$$

The expression in square parenthesis in Equation 2.30 can be expanded using the binomial theorem as given:

$$\left[1 + \frac{4(\omega_1 - \omega(q))^2}{\Gamma_0^2}\right]^{-1} = \left[1 - \frac{4(\omega_1 - \omega(q))^2}{\Gamma_0^2} + \left[\frac{4(\omega_1 - \omega(q))^2}{\Gamma_0^2}\right]^2 - \left[\frac{4(\omega_1 - \omega(q))^2}{\Gamma_0^2}\right]^3 \pm \ldots\right] \tag{2.31}$$

Insertion of the acoustic (−) and the optical (+) phonon dispersion relation of a general

nature as

$$\omega(q) = A \pm Bq^2 \tag{2.32}$$

(see Appendix 2 for the choice of this form of the phonon dispersion relation) in Equation 2.31 and further expansion leads to

$$\left[1 + \frac{4\left(\omega_1 - \omega(q)\right)^2}{\Gamma_0^2}\right]^{-1} = 1 - \left[\epsilon\alpha_0 q^0 + \epsilon\alpha_2 q^2 + \epsilon\alpha_4 q^4 + \epsilon\alpha_6 q^6 + \ldots\right] \tag{2.33}$$

where

$$\epsilon = \frac{4}{\Gamma_0^2} + \left(\frac{4}{\Gamma_0^2}\right)^2 + \left(\frac{4}{\Gamma_0^2}\right)^3 + \ldots \tag{2.34}$$

and

$$\begin{aligned}
\alpha_0 &= (\omega_1 - A)^2 + (\omega_1 - A)^4 + (\omega_1 - A)^6 + \ldots \\
\alpha_2 &= -2B(\omega_1 - A) - 4B(\omega_1 - A)^3 - 6B(\omega_1 - A)^5 - \ldots \\
\alpha_4 &= B(\omega_1 + A)^0 + 6B(\omega_1 + A)^2 - 15B(\omega_1 + A)^4 + \ldots \\
\alpha_6 &= -4B(\omega_1 - A) - 20B((\omega_1 + A))^3 - \ldots \\
\alpha_8 &= B + 15B(\omega_1^2 - A^2) + \ldots \\
\alpha_{10} &= -6B(\omega_1 - A) \\
\alpha_{12} &= B + \ldots
\end{aligned} \tag{2.35}$$

Having successfully done the binomial expansion, it is now easier to perform the integral in Equation 2.30 but this can only be achieved by a change of variables from q to ϱ in spherical co-ordinates as follows:

$$\int_0^\infty d^3q = 2\pi \int_0^\pi sin\psi d\psi \int_0^\infty \varrho d\varrho = 4\pi \int_0^\infty \varrho d\varrho \tag{2.36}$$

$$q^2 = \frac{1}{3}\varrho^2 \tag{2.37}$$

Equations 2.36 and 2.37 are substituted into Equation 2.30 and the integral is evaluated

bearing in mind the standard integrals

$$\begin{aligned}
&\textstyle\int_0^\infty x^n e^{\nu x^2} dx = f(n) \\
&f(0) = \sqrt{\tfrac{\pi}{\nu}} \\
&f(1) = \tfrac{1}{2\nu} \\
&f(2) = \tfrac{1}{4}\sqrt{\tfrac{\pi}{\nu^3}} \\
&f(3) = \tfrac{1}{2\nu^2} \\
&f(4) = \tfrac{3}{8}\sqrt{\tfrac{\pi}{\nu^5}} \\
&f(5) = \tfrac{1}{\nu^3}
\end{aligned} \tag{2.38}$$

This then transforms Equation 2.30 to the following

$$I(\omega_1) = \Gamma_0 \int_0^\infty e^{-\frac{d^2\varrho^2}{12\pi^2}} \left[1 - \epsilon\alpha_0 - \frac{1}{3}\epsilon\alpha_2\varrho^2 - \frac{1}{3}\epsilon\alpha_4\varrho^4 - \frac{1}{3}\epsilon\alpha_6\varrho^6 - \ldots\right] d\varrho \tag{2.39}$$

which upon evaluation gives

$$\begin{aligned}
&I(\omega_1) = \Gamma_0 \left[\tfrac{\gamma_1}{d} - \tfrac{\gamma_3}{d^3} - \tfrac{\gamma_5}{d^5} - \tfrac{\gamma_7}{d^7} - \ldots - \tfrac{\gamma_{2i+1}}{d^{2i+1}}\right], \qquad i \in \aleph \\
&\gamma_1 = (1 - \epsilon\alpha_0)\,\pi\sqrt{12\pi} \\
&\gamma_3 = \epsilon\alpha_2\pi^3\sqrt{12\pi} \\
&\gamma_5 = 12\epsilon\alpha_4\pi^5\sqrt{12\pi} \\
&\gamma_7 = 576\epsilon\alpha_6\pi^7\sqrt{12\pi}
\end{aligned} \tag{2.40}$$

This equation suggests that as d$\longrightarrow\infty$

$$I(\omega_1) \longrightarrow \tfrac{\Gamma_0\gamma_1}{d}, \qquad bulk \tag{2.41}$$

Most authors have used Raman intensity versus the inverse of grain diameters only empirically and have tried to convince readers that what they obtain are linear fittings. What has been in all this theoretical ramification is a ground- breaking evidence of the experimental findings that many researchers take for granted. The immense celebration however is only limited to the fact that the linearity in Raman intensity and inverse of grain diameter only applies when one neglects the higher terms in Equation 2.43 and only considers the first term. Non-linearities are clearly apparent when one includes the higher terms and this, more often than

not, is the reality. So, based on Equation 2.43, the practice of plotting Raman intensity versus the inverse of cluster diameter is more appropriate for larger cluster systems (bulk) than nanometric grains. That is, another simplification is required to characterize nanometric grains.

This chapter began with the need to quantify the assertion that the ratio of the integrated Raman intensities of neighboring peaks can be used to give a measure of the amount of cluster size. This is proposed in this dissertation as a means of directly extracting information pertaining to phonon dispersion relations for materials.

Since one of the integrated intensities, which is a numerator in Equation 2.28, has already been worked out, it is possible to write the other integrated intensity, the denominator, in the same form as in Equation 2.43 with all the γ's replaced by a different symbol, say, μ. Then the ratio of the integrated intensities of the peaks 1 and 2, $\Pi_{1,2}$, can be written as:

$$ {}_1\Pi_2 = \frac{\frac{\gamma_1}{d} - \frac{\gamma_3}{d^3} - \frac{\gamma_5}{d^5} - \frac{\gamma_7}{d^7} - \ldots - \frac{\gamma_{2i+1}}{d^{2i+1}}}{\frac{\mu_1}{d} - \frac{\mu_3}{d^3} - \frac{\mu_5}{d^5} - \frac{\mu_7}{d^7} - \ldots - \frac{\mu_{2i+1}}{d^{2i+1}}} \tag{2.42} $$

In this case, the μ's take the similar form as the γ's as follows:

$$ \begin{aligned} \mu_1 &= (1 - \epsilon\beta_0)\,\pi\sqrt{12\pi} \\ \mu_3 &= \epsilon\beta_2\pi^3\sqrt{12\pi} \\ \mu_5 &= 12\epsilon\beta_4\pi^5\sqrt{12\pi} \\ \mu_7 &= 576\epsilon\beta_6\pi^7\sqrt{12\pi} \end{aligned} \tag{2.43} $$

where similarly

$$ \epsilon = \frac{4}{\Gamma_0^2} + \left(\frac{4}{\Gamma_0^2}\right)^2 + \left(\frac{4}{\Gamma_0^2}\right)^3 + \ldots \tag{2.44} $$

and

$$\begin{aligned}
\beta_0 &= (\omega_2 - A)^2 + (\omega_2 - A)^4 + (\omega_2 - A)^6 + \ldots \\
\beta_2 &= -2B(\omega_2 - A) - 4B(\omega_2 - A)^3 - 6B(\omega_2 - A)^5 - \ldots \\
\beta_4 &= B(\omega_2 + A)^0 + 6B(\omega_2 + A)^2 - 15B(\omega_2 + A)^4 + \ldots \\
\beta_6 &= -4B(\omega_2 - A) - 20B((\omega_2 + A))^3 - \ldots \\
\beta_8 &= B + 15B(\omega_2^2 - A^2) + \ldots \\
\beta_{10} &= -6B(\omega_2 - A) \\
\beta_{12} &= B + \ldots
\end{aligned} \tag{2.45}$$

Multiplying both the numerator and denominator in Equation 2.42 by the d in the last term gives an alternative expression for the ratio as

$${}_1\Pi_2 = \frac{\gamma_1 d^{2i} - \gamma_3 d^{2i-2} - \ldots \gamma_{2i+1}}{\mu_1 d^{2i} - \mu_3 d^{2i-2} - \ldots \gamma_{2i+1}} \tag{2.46}$$

and, upon polynomial division, the Equation 2.46 can be re- written to

$${}_1\Pi_2 = \frac{\gamma_1}{\mu_1} + \frac{\left(\gamma_1 \frac{\mu_3}{\mu_1} - \gamma_3\right) d^{2i-2} - \gamma_1 \left(\frac{\mu_5}{\mu_1} - \gamma_5\right) d^{2i-4} - \ldots \left(\gamma_1 \frac{\mu_{2i+1}}{\mu_1} - \gamma_{2i+1}\right)}{\gamma_1 d^{2i} - \gamma_3 d^{2i-2} - \ldots \gamma_{2i+1}} \tag{2.47}$$

or in shorthand to

$${}_1\Pi_2 = \frac{\gamma_1}{\mu_1} + \frac{\sum_{i,j}^{\infty} \left(\gamma_1 \frac{\mu_{2k+1}}{\mu_1} - \gamma_{2k+1}\right) d^{2i-2(k+1)}}{\mu_1 d^{2i-2} - \sum_{i,j}^{\infty} \mu_{2k+1} d^{2i-2(k+1)}} \tag{2.48}$$

This equation as opposed to Equation 2.43 show that as d $\longrightarrow$ 0 only some values of i and j are allowed. The lowest allowable values are i=2 and j=1. Hence one gets

$${}_1\Pi_2 = \frac{\gamma_1}{\mu_1} + \frac{\frac{\gamma_1}{\mu_1}\frac{\mu_3}{\mu_1} - \frac{\gamma_3}{\gamma_1}}{d^2 - \frac{\mu_3}{\mu_1}} \tag{2.49}$$

For $d^2 \gg \mu_3/\mu_1$, one gets

$${}_1\Pi_2 = \frac{\gamma_1}{\mu_1} + \left(\frac{\gamma_1}{\mu_1}\frac{\mu_3}{\mu_1} - \frac{\gamma_3}{\mu_1}\right)\frac{1}{d^2}, \qquad nano \tag{2.50}$$

This equation now shows that the simplification of the relationship between ${}_1\Pi_2$ and cluster size can only be possible if higher terms are neglected. That is, the ratio in Equation 2.47 tends only to inverse of d for very small (nanometric) grains and a plot of ${}_1\Pi_2$ versus the inverse of d^2 becomes more linear when grain diameters are in nano-meter regions. This then means that this Equation 2.50 can be more appropriate for characterization of nanometric grains and Equation 2.43 would be good for bulk.

2.3 PC model linearization, size distribution and phonon dispersion relations

The present proposed linearization of the phonon confinement model brings out two major benefits:

1. If one has phonon dispersion relations for the material one is studying at hand, normally obtained from neutron scattering, then it is possible to use the PC model, especially the present linearization of it (Equations 2.41 and 2.50), to estimate the sort of size distribution of the material particles. However, due to a scarcity of these phonon dispersion relations for many new materials, most materials researchers opt to use phonon dispersion relations from analogous materials thus introducing some errors in their analyses.

2. On the other hand, sufficient knowledge of the size distribution of the materials under study, obtained by scanning electron microscopy or tunneling electron microscopy, would enable one to use the present linearization of the PC model to approximately determine the phonon dispersion relations for that material. This study therefore introduces a very important tool for acquiring dispersion relations by Raman spectroscopy for material that would otherwise not qualify for neutron scattering. Materials such as vanadium dioxide and a number of transition metal oxides are said to have very large neutron scattering angles and thus render themselves difficult material with regard to neutron scattering. To this end, Raman spectroscopy and especially the present

linearization of the PC model offers a simple method for obtaining this important information.

In this discussion, considering Equation 2.41 and substituting all components for ϵ and α_0 yields the following expression:

$$I(\omega_1) = \frac{\Gamma_0 \pi \sqrt{12\pi}\left[1 - \left\{\frac{4}{\Gamma_0^2} + \left(\frac{4}{\Gamma_0^2}\right)^2 + \left(\frac{4}{\Gamma_0^2}\right)^3 + \ldots\right\}\left\{(\omega_1 - A)^2 + (\omega_1 - A)^4 + (\omega_1 - A)^6 + \ldots\right\}\right]}{d} \tag{2.51}$$

In the above Equation 2.51, if a plot of Equation 2.51 with d^{-1} on the x-axis is made, it will give the numerator as the slope of the graph and the slope is more likely to be negative as seen in the equation. This confirms the present findings as presented in the results chapter.

If the slope of this graph is represented as S_{bulk} and only the first terms are considered in the equation then S_{bulk} can be written as

$$S_{bulk} = \Gamma_0 \pi \sqrt{12\pi}\left[1 - \frac{4(\omega_1 - A)^2}{\Gamma_0^2}\right] \tag{2.52}$$

and it is possible to factor out one component of the phonon dispersion relation, A, as given in Equation 2.53

$$A = \omega_1 \pm \sqrt{\omega_1^2 - \left[\omega_1 - \frac{1}{2}\left(1 - \frac{\Gamma_0 S_{bulk}}{\pi\sqrt{12\pi}}\right)\right]}, \qquad bulk \tag{2.53}$$

This means that for the case of bulk-material PC model linearization, only one component of the phonon dispersion relation can be obtained.

However, if the same analysis is done to the equation for nanometric materials as given in Equation 2.50 by first substituting all the components of the variable symbolized as γ and μ, one obtains the following:

$${}_1\Pi_2 = \frac{1 - \epsilon\alpha_0}{1 - \epsilon\beta_0} + \left(\frac{\epsilon\beta_2\pi^2}{1 - \epsilon\beta_0} - \frac{\epsilon\alpha_2\pi^2}{1 - \epsilon\alpha_0}\right)\frac{1}{d^2} \tag{2.54}$$

A plot of Equation 2.54 against d^{-2} will give an intercept, C, of the following form:

$$C = \frac{1 - \epsilon\alpha_0}{1 - \epsilon\beta_0} \tag{2.55}$$

After substituting the first terms only (as before) of ϵ, α_0 and β_0 into Equation 2.55 and performing a bit of algebra, an expression for the first component of the phonon dispersion relation, A, for the nanometric case is obtained and given as

$$A = \frac{\left[-(\omega_2 C - \omega_1) \pm \sqrt{(\omega_2 C - \omega_1)^2 - (1-C)\left\{\omega_1^2 - \omega_2^2 C - \frac{\Gamma_0^2}{16}\right\}}\right]}{2(1-C)}, \qquad nano \tag{2.56}$$

Also from a plot of Equation 2.54 a second simultaneous equation is obtained from the slope (symbolized as M) given as

$$M = C\epsilon\pi^2 \frac{\beta_2 - \alpha_2}{1 - \epsilon\beta_0} \tag{2.57}$$

After the similar substitution, the following expression for the second parameter in the phonon dispersion relation is found:

$$B = \frac{M\Gamma_0^2}{8\pi^2}\left(\frac{1 - 4\Gamma_0^{-2}(\omega_2 - A)^2}{(\omega_1 - A)} - C(\omega_2 - A)\right) \tag{2.58}$$

With A already known from Equation 2.56, then the second parameter in the phonon dispersion relation, B, can also be calculated.

Chapter 4 illustrates how this approach has been used in the present study to obtain phonon dispersion equation for tungsten trioxide.

Chapter 3

Experiments

Precursors of ammonium metavanadate, NH_4VO_3 (coded AMV), ammonium metavanadate mixed with vanadium trichloride, NH_4VO_3 + VCl_3 (coded AMVC), and ammonium metatungstate hydrate, $(NH_4)6W_7O_{24}.6H_2O$ (coded AMTH) were prepared in different concentrations. The AMV was a whitish yellowish powder with molecular weight of 116.98, density of 2.326 g/cm^3 and a melting temperature of 200^{o}C. Similarly, the AMTH was a white powder with molecular weight of 1887.19 density of 3.294 g/cm^3 and melting temperature of 470^{o}C.

Scoops weighing 6.0 g and 4.1 g of AMV and AMTH respectively were dissolved in 600ml of distilled water and mixed well using a magnetic stirrer on a hot plate at around 70^{o}C. The so-made solutions were one after the other then decanted into the container that was housing the ultrasonic nebulizer operating at a frequency of 1.7MHz as illustrated in the schematic diagram of Figure 3.1 A photograph of our USP system under operation is given in Figure 3.1(b) and a schematic set up is illustrated in Figure 3.1(a)

This consisted of the ultrasonic nebulizing unit, the furnace unit (The furnace was a REX D100 supplied by RKC Instrument Inc., Tokyo, Japan), the carrier gas unit and the exhaust system. The ultrasonic nebulizer was composed of seven piezoelectric transducers driven at a frequency of 1.7 MHz by a ultrasonic generator supplied by TDC Power Products Co. Ltd, Germany shown in Figure 3.2

Substrate materials underwent the usual rigorous cleaning procedure of detergent- ultrasonic

bath- alcohol ultrasonic bath until the substrates qualified for deposition. A DeContam^{TM} and Cleen Green^{TM} detergents supplied respectively by Electronic Space Products International and Wynn Oil South Africa (Pty) Ltd were used. The ultrasonic bath was one of Elma Transsonic supplied by Elma Hans Schmidbauer GmbH & Co5, Germany illustrated in photograph labelled as Figure 3.3

Depositions were done on different types of substrates, at various furnace temperatures, at various substrate positions in the furnace and various carrier gas conditions. A number of VO_2 samples were prepared from NH_4VO_3 solution using the highest flow rate the flow meter could allow and making deposition for 40 minutes. With these setting only temperature of decomposition was varied between 400^oC and 700^oC. It was observed that the precursor solution temperature also changed- from 23 to 85^oC. The substrate material quartz was chosen for its high temperature tolerance and these substrates were carefully placed evenly along the quartz tube that was running through the furnace. For other substrates- borosilicate and Corning glass- these were placed at the exit of the furnace. Other carrier gases such as hydrogen and oxygen were also tried in order to study the effect of the nature of the carrier gas. Flow rates were also varied to optimize the best flow rate from as high as 18 liter per minute to about 8 liters per minute. Samples in this category of synthesis were labeled as V1, V2, V3 up to V10. The other category of samples was arrived at by finding out the weakness in the former precursor solution. This was after X-ray diffraction and thermochromism experiments on the VO_2 samples in the former had shown presence of small amounts of VO_2 overshadowed by V_2O_5. In the latter category, it was decide the precursor was to be enriched with VCl_3 so that the valence of VO_2 was satisfied. With the argon flowrate optimized at 11 liters per minute interesting properties of VO_2 were clearly apparent in this category.

As for the deposition of WO_3, the same optimization procedures were followed as those for VO_2. In this last category, the interest was not focused on obtaining WO_3 as such but producing various sizes of the grains on the samples bearing in mind the WO_3 applications of gas sensing. To obtain varying structural and morphological texture in the WO_3 sample, the temperature of the deposition process was carefully regulated and varied from 100 to 700^oC. The samples, labeled W1, W2, W3 up to W7 showed very interesting optical and structural properties as presented in the results chapter.

Structural studies of the as- deposited nano-particles were done using a Powder X-ray Diffractometer with a Cu K_α wavelength of 0.154184 nm

The rotating anode in Figure 3.4 is a copper target which decelerates the incident electrons which in turn emit "primary" X-rays. These rays are then focused onto the crystal (sample) set on a slowly rotating stage (2θ variable). The speed of rotation determines the scan rate of the X-ray diffractometer. The detector can be an area-type of detector or an intensity sensor that can convert the value of intensity into a current or voltage which is then datalogged by a computer, through appropriate software, for a plot of intensity versus 2θ.

Optical properties of transmittance or absorbance were conducted using a VARIAN CARY UV-Vis-IR spectrophotometer illustrated in Figure 3.5. This was done to ascertain the amount of switching capability of the as- prepared samples at and around the VO_2 transition temperature (68^oC).

The scanning electron microscope (SEM) that was used in this study was a Jeol JSM-5600 type. (The SEM in general creates the magnified images by using electrons instead of light waves. The SEM shows very detailed 3-D images at much higher magnifications than is possible with an optical microscope. Samples have to be prepared carefully in order to withstand the vacuum inside the microscope. Because the SEM illuminates them with electrons, the samples also have to be made to conduct electricity. In this case, the VO_2 and WO_3 samples were coated with a thin film of carbon of thickness of about 1 nm per cm^2. Between the electron gun and the sample was placed a high voltage source, typically, about 15kV, in these experiments. After the air was pumped out of the column, an electron gun [at the top] emitted a beam of high energy electrons. This beam traveled downward through a series of magnetic lenses designed to focus the electrons to a very fine spot. Near the bottom, a set of scanning coils moved the focused beam back and forth across the specimen, row by row. As the electron beam hit each spot on the sample, secondary electrons would be knocked loose from its surface. A detector counted these electrons and sent the signals to an amplifier. The final image was built up from the number of electrons emitted from each spot on the sample.)

A typical SEM set up similar to the one used in this study is illustrated in Figure 3.6

Analysis of SEM images was carried out using Image Tool^{TM}. This is a free software downloadable from the internet but has features like scanning the image surface for objects, counting, measuring diameters, perimeters, calculating area and many more parameters. The definition of the parameters contained in Image Tool^{TM} are presented in the first appendix. To properly interpret the images and to accurately measure the particle sizes, there was need to be sure of the relationship between the attributes that are featured on and accompanies each SEM image: that is, micron marker (L_{SEM}) in μm, the magnification (M_{sem}) and the measured length of the micron marker (L_{mm}) in mm. We got the best linear relationship when the data obtained followed the fitted line

$$\frac{L_{mm}}{L_{SEM}}\left(4.0M_{sem} - 124\right) \times 10^{-4} \tag{3.1}$$

with coefficient of correlation of r^2=0.9998 an indication of almost 100% correlation.

The linearity in the relationship between spatial measurement ratios and SEM magnification gave a clue that the manual measurement l_{pixel} in the image analysis software, Image Tool^{TM}, followed the same relationship which was found to be

$$\frac{l_{pixel}}{l_{SEM}} = 0.00512M - 0.16 \tag{3.2}$$

With these calibration procedures in place image analysis of our so- obtained scanning electron microscopy images were completed. The results of these analyses are presented in the Chapter Four.

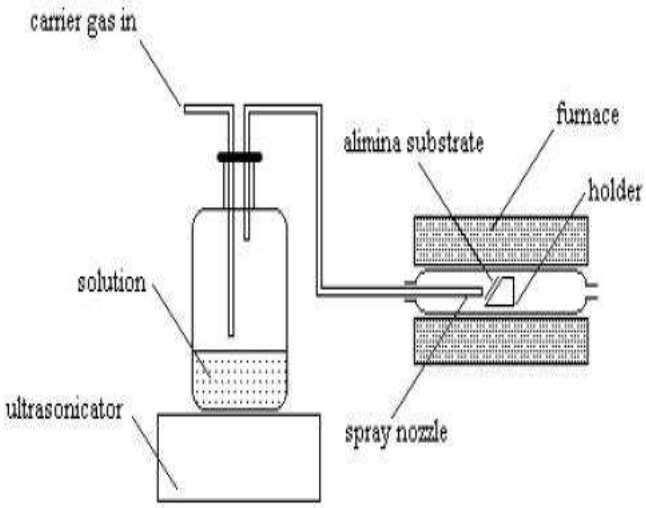

(a)

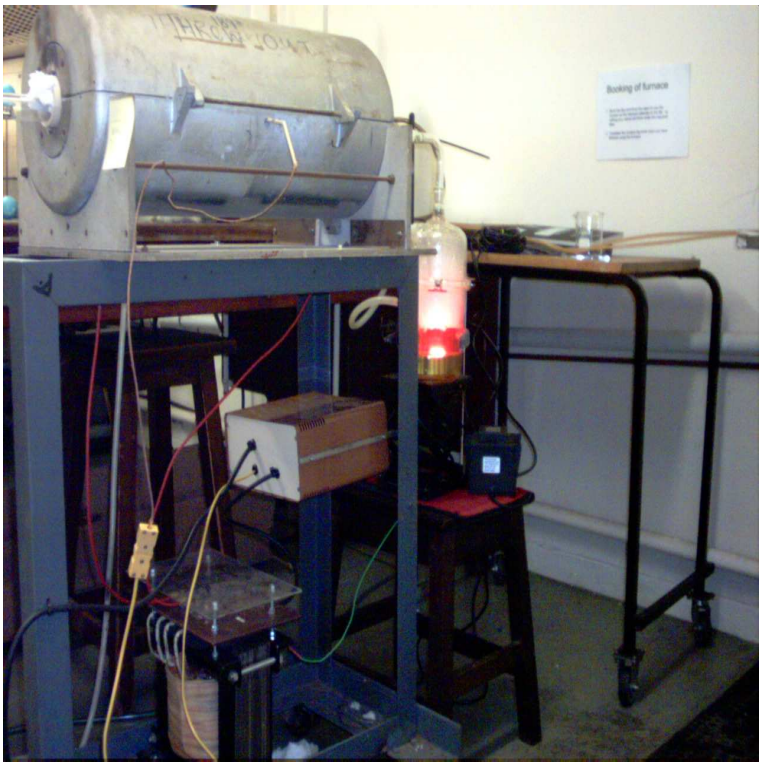

(b)

Figure 3.1: A schematic representation of the ultrasonic nebulizing spray pyrolysis technique and a photograph of the system used in the present work

Figure 3.2: A photograph of the ultrasonic transducer that was used to produce droplets through out the present study


(a)
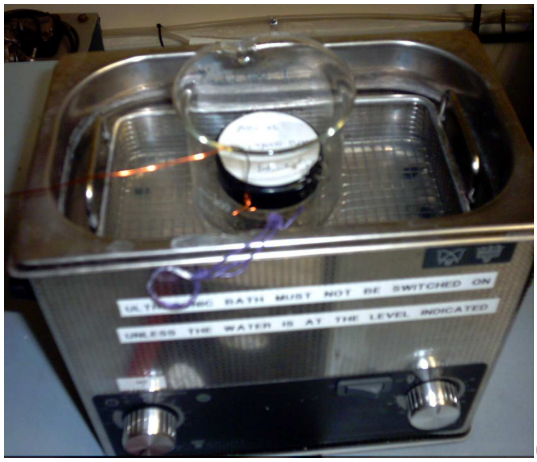
(b)

Figure 3.3: A photograph showing (a)the work table with starting materials and other allied equipment (b) the ultrasonic bath where subtrate could be cleaned before deposition

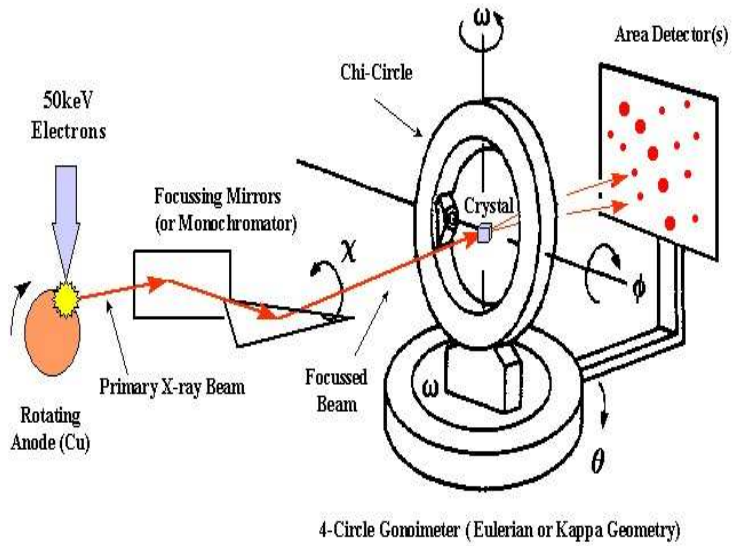

Figure 3.4: A schematic illustration of the pertinent components of a standard X-ray diffractometer

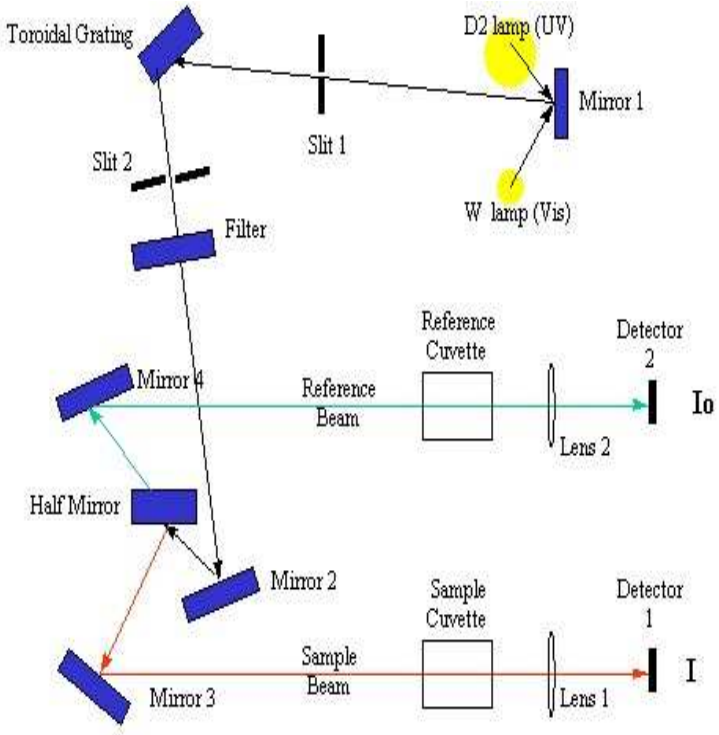

Figure 3.5: A layout of a standard spectrophotometer for analysis of electromagnetic radiation in the UV-Visible-IR regions.

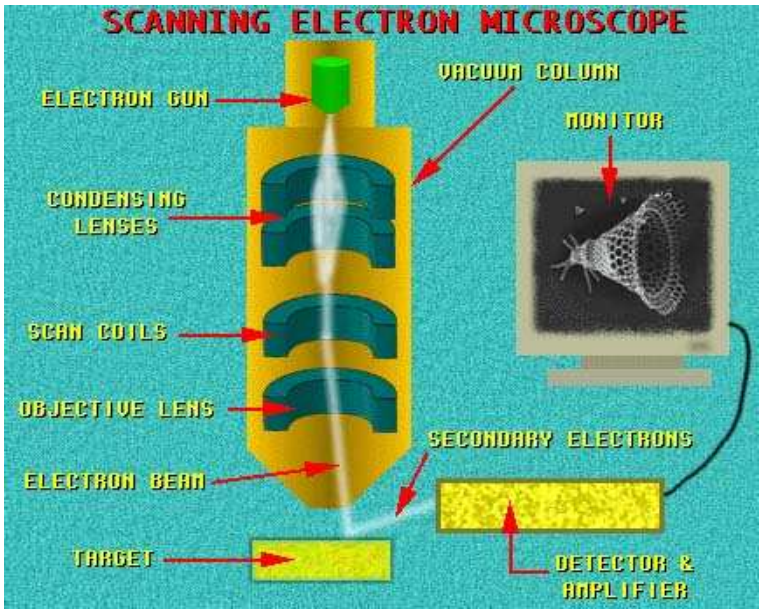

Figure 3.6: An illustration of a typical scanning electron microscope that was employed in the present study

Chapter 4

VO_2 and WO_3 characterization results

In this chapter, findings on the present attempt to resolve the conflict between measured and calculated grain sizes obtained by ultrasonic spray pyrolysis on various materials are presented. Also the data from the present work are included in the analyses. Also outlined are the characterization results from the VO_2 and WO_3 samples- X-ray diffraction, UV-Vis-IR spectroscopy, Scanning electron microscopy and other pertinent observations.

4.1 Size of droplets and the resulting grains and the Lang-Jokanovic models

Comparisons of calculated and measured grain sizes are best presented by plot a scatter graph with each parameter on each axis as illustrated in Figure 4.1 and Figure 4.2. Data pairs from each author are plotted on these charts and compared with the ideal straight. Any data pairs falling on this ideal imply that their calculated grain size is exactly equal to their measured size.

From the pool of over seventy publications [93] $\rightarrow$ [169], all the data on experimental and calculated grain sizes have been compared and relationships have been found between calculated particle sizes and those obtained either from scanning electron microscopy using image analysis techniques or X-ray diffraction using the Scherrer equations 1.12 and 1.13 in Chapter

One.

Whether one uses the Lang or the Jokanovic equation to calculate the grain sizes, the measured sizes are always a distribution around a mean size. The standard deviations give the amount of spread and, within experimental error in line with Equation 2.4, most previous findings are outside the allowed regions as the graph in Figure 4.1 shows. Also, a number of authors reviewed did not give enough information about either how the so- declared grain sizes were obtained or the pertinent data, such as frequency, density of surface tension, required to calculate the sizes in cases where these sizes are not pre- given. For instance, during the review process, it was imperative to contact one of the previous authors, Dr F Attay [107],[109], to get data on density, concentration, droplet distribution, ultrasound frequency and other kinds of data.

Above all, the charts in Figures 4.1 and 4.2 show that most researchers have so far been very far away from the ideal case of calculated diameters by Jokanovic and/or Lang model being equal or in the neighbourhood of the measured diameters. These previous discrepancies prompted the present refinement of the Jokanovic and Lang models as presented in Chapter Two.

The present refinement has shown that droplets, from where the resulting grains/ particles are obtained, shrink in size as the temperature of the precursor and the pressure of the USP system rise. The droplet-temperature and droplet-pressure profiles are however slightly different. For the former case, the droplet diameter decreases at an increasing rate as temperature rises from room to about boiling point of the precursor. The present model estimates that from room temperature to boiling point, the diameter falls by about 16.7 percent of the original diameter. However, the choice of the type of model equation to use is crucial. The difference in calculated droplet diameter between using Jokanovic and Lang equation turns to be a factor of an awesome 68 percent. This is shown in each graph in Figure 2.1, 2.2 and 2.3. The droplet diameter-pressure profile in Figure 2.2 similarly shows a decrease in droplet diameter as pressure rises from a little below atmospheric pressure to slightly above. The droplet shrinkage, in contrast to that of precursor temperature, decreases at a decreasing rate. Also the droplet shrinkage is estimated to be by a factor of 14 per cent of the original diameter in the neighbourhood of atmospheric pressure. This means that precursor tempera-

ture has more effect than pressure in general. At the time of writing this dissertation, recent data from Parent et al (2005) [89] [89] and Hopkins et al (2005)[90], respectively on droplet-pressure and droplet size- temperature, were encoporated to validate the finding. Fitting of the present model to these data is presented in Figure 4.3

The most interesting parameter and which requires scientific explanation is the volume either of the USP system or that occupied by the droplet; which ever terminology fits the description of V in the model. In Figure 2.3, the sharp increase of droplet diameter as volume increases especially around 0.1 m^3 is still a subject of discussion and this is an inexplicable phenomenon. However, this sharp increase in droplet sizes with the volume they occupy has been observed in droplets generated by electrostatic means by Priol et al [91]. In their observation, they used a Malvern's Spraytec system to measure the size of the droplets. The system was designed for real-time high-speed measurements running at a time-resolution of 400 micro-seconds and fully automated. The size measurement system is based on Mie theory. The illuminated droplet scatters light such the scattered light's intensity and amount of scatter gives information about the size of the droplet. Priol et al (2005) first compared the size distributions of two different injectors: one with length-diameter (L/D) ratio of 2 and the other of 10. In the latter case, they found that the so- produced jet had more droplets with diameters of 100 microns, whereas for the one with L/D of 2, "...25 per cent of the total volume is occupied by droplets which have a maximal diameter of 65 micrometers..." In short, what Priol et al found is that small droplet tend to occupied small volume and the reverse is true for large droplet. To put it the other way round, large volumes tend to contain large droplets whereas small volumes tend to contain small droplet. One of the charts Priol et al (2005) presents is reproduced in Figure 4.4

4.2 Optical measurements of the VO_2 and WO_3 samples

It is interesting to note that furnace temperature and the nature of the carrier gas have such a great effect on the nature of deposited nano- particles. At low temperatures, the deposits

from the meta-vanadate precursor had yellow color; at high temperatures the colors shifted to bluish, gray and blue- black. The same applied to the deposits from meta- tungstate: from white at low temperatures to yellow at high temperatures.

UV-Vis-IR transmittance spectroscopy is useful in revealing the switching properties of VO_2 from the room temperature monoclinic structure to a tetragonal rutile-type structure at above 68^oC. Very small amount of switching was observed in samples prepared from a precursor of NH_4VO_3 with carrier gases of argon or hydrogen or oxygen.

The samples prepared using NH_4VO_3 enriched with VCl_3 had a remarkable switching improvement when transmittance was measured at different ambient temperatures. Typical transmittance thermal-modulation curves are represented in Figure 4.5 during heating and cooling. The sample V13 synthesized at 600^oC under argon shows a transition temperature around 60^oC and a switching temperature resolution of HW = 20^oC (as shown in the hysteresis plots in Figures 4.6) not only reveals the crystal quality but also signifies the broadening possibly due to particulate size. The switching contrast is significantly reduced in the sample synthesized at 700^oC (V14) as expected where the particulate size is supposedly larger than on the V13 sample (Figure 4.7). The V15 sample shows an average resolution of about 7^oC. One can also easily see the relationship between switching factor of a sample and the temperature at which it was synthesized.

A completely different transition is observed in the VO_2 sample prepared at 700^oC but under oxygen. A transition temperature of around 23^oC can clearly be seen as illustrated in Figure 5.3. The role of oxygen in the change of properties is suspected but also a slight effect of tungsten from the remnants of the ammonium metatungstate precursor at preparation and handling stages might be responsible for this shift in transition temperature.

4.3 VO_2 and WO_3 crystal structure confirmation by X-ray diffraction experiments

X-ray diffraction revealed very prominent peaks belonging to VO_2 crystal faces such as (100), (110) and (011) in a sample prepared on window glass at 700^oC as illustrated in Figure

4.9. This suggests the VO_2 crystallites are randomly ordered rather than preferring some direction. Hydrogen carrier gas tends to bring other phases of VO_2. In all cases in this group of samples, the presence of other phases inhibits the manifestation of the VO_2 properties hence the switching factor so observed.

It is also worth observing that the temperature of deposition affects the morphology of the as-deposited particles. This can be seen in the appearance of sharper and more prominent peaks as temperature of deposition is increased.

For tungsten trioxide, it was observed that it was much easier to obtain WO_3 from its precursor aqueous solution of $(NH_4)_6W_7O_{24}.6H_2O$ than to obtain VO_2 due to fewer phases of tungsten oxides. The only possible phase known is WO_2 which is not stable. The most stable phase amongst tungsten oxides is WO_3 whereas, among vanadium compounds, there is V_2O_5 as the most stable. The same effect of synthesis temperature was also seen on the morphology and crystallinity of WO_3. This can be seen from the absence of prominent X-ray peaks in a sample prepared at 400^oC in Figure 4.10.

In order to characterize the morphology of the particulates and crystallites on the so- obtained samples, the Scherrer equation (Equation 1.12 and 1.13) in Chapter 1 was employed to estimate the particulate sizes. This analysis confirmed the initial expectations that the present work's crystallites would have sizes in the nanometer scale.

4.4 VO_2 and WO_3 phonon signatures by Raman spectroscopy

4.4.1 Raman spectroscopy results for VO_2

A number of authors have published their Raman study findings in various forms of VO_2 whether crystalline, amorphous or singe crystals. Raman intensities are much higher from crystals. However, little is done in nanometric powders due to the weakness of the Raman signal from these samples. In this work intensity of the exciting laser had to be set at a considerable amount in order to get some signal from our nano-metric samples. At about

x200 magnification, one could see that the so-prepared samples were amorphous mixed with islands of single crystals. In Table 4.1 these previous findings are presented alongside the present findings.

From the table, it is found out that the present work's data matches with most previous findings conducted at room temperature. In fact, the present work supersedes most of the previous studies in as far as the ability to observe phonon modes having lower and much higher Raman frequency shifts is concerned. Any observed differences in characteristic wavenumbers and their assignment among authors in Table 4.1 is seen to be due to several factors: (1) sample preparation differences, (2) some were taken at room temperature where others carried out Raman measurements at low temperatures, (3) machine type differences including the type of laser used for sample excitation.

4.4.2 Raman spectroscopy results for WO_3

In their Raman spectra of WO_3 for the temperature range from 100K to 650K, Gabrusenoks et al (2001)[80] noted that the phonon activity may be grouped in a set of two ranges: high at 600-800 cm^{-1} and low at 30-400cm^{-1} and this, in agreement with previous investigations is attributed to successive deformation of the cubic lattice giving rise to the observed Raman activity of phonons. Gabrusenoks et al (2001)[80] also reiterate the fact that from group theoretical analysis of the "wolframite..." the structure with $C4_{2h}$ (P2/c) space group gives the distribution of the vibrations into the irreducible representation as

$$\Gamma = 8A_g + 10B_g + 7A_u + 8B_u \tag{4.1}$$

where A_g and B_g are Raman active while A_u and B_u are infrared active.

Lee et al (2001)[84] found a relatively sharp peak at 950 cm^{-1} which they attributed to the W^{6+}=O stretching mode of terminal oxygen atoms (possibly on the surface of the WO_3 cluster and micro-void structures in the film. A broad peak at 770 cm^{-1} was attributed to the O-W^{6+}-O bonds whereas a weaker and broad band at 220cm^{-1} was seen as resulting from W^{4+} states. These are similar observations made by Huang et al[81] wherein 756 and 895 cm^{-1} peaks are seen to be due to the O-W^{6+}-O vibrations and 230 cm^{-1} peak is simply

labeled as a Raman excited peak; no sharp peak around 950 cm^{-1} is reported by Huang et al (2002) which usually is assigned to the W^{6+}=O stretching mode in amorphous WO^3. On hydrogen insertion in which case W^{6+} entities are reduced by e^{-s} to W^{5+}, two new peaks are seen by Lee et al (2001)[84] at 330 and 450 cm^{-1} at the expense of the intensities of the 770 and 950 cm^{-1} peaks respectively. On the other hand, Huang et al (2002)[81] observe three new peaks on Li^+ insertion: 315, 410 and 680 cm^{-1} which they attribute to the O-W^{5+}-O vibrations. This discussion is fully treated in the conclusion chapter. The present work's Raman spectra for WO_3 synthesized at temperatures of 100 to 700^{o}C are presented in Figure 4.13. These spectra confirm previous findings and as for VO_2 spectra the present work has enabled observations in Raman shifts much lower and much higher than observed before, that is, shift peaks lower than 100 cm^{-1} and higher than 960 cm^{-1}.

4.5 Surface morphology of the VO_2 and WO_3 samples by scanning electron microscopy(SEM)

4.5.1 SEM for VO_2

Interesting morphology results are presented in a sample micrograph gallery in Figures 4.11. This is scanning electron microscopy (SEM) snapshot showing the size distribution of the particles of VO_2 synthesized at 600^{o}C.

4.5.2 SEM for WO_3

Images of WO_3 samples synthesis at different system temperatures suggest an obvious relationship between the resulting grain sizes and the substrate temperature. The grains when analyzed using Image Tool, show very fine, nanometeric size at low substrate temperatures and generally plate-like structures of micro-meter size at high substrate temperature.

An even more interesting quantitative relationship between grain size and substrate temperature is apparent when a chart of mean feret diameter of grain versus substrate temperature

is plotted. From Figure 4.12, it can be seen that most of the grain increase in size with an exponential growth as substrate temperatures are raised whereas another set of grains either remain unperturbed or shrink in size.

This is attributed to both growth (due to nano-grains coalescing to form bigger grains) and evaporation of some material from those grains that have not had the chance to coalesce with neighboring grains. The plate-like structure is certainly due to melt down of some of the large grains as substrate temperatures are raised.

4.6 Estimation of phonon dispersion relations for WO_3 from the linearized PC model and SEM results

From the the SEM results of size controlled WO_3 samples, an almost definite size distribution was obtained as seen from Appendix 3 from page 112 of this dissertation. Having established the relationship between grain size and substrate temperature, it is then possible, from Raman spectra of each class of grains, to correlate either intensity of some phonons in the grains to the temperatures of synthesis and consequently their sizes. Intensity values of the phonons were found by fitting a Gaussian to each Raman peak for each sample. Peaks at Raman frequencies 700 cm^{-1}, 804 cm^{-1} and 960 cm^{-1} were fitted with Gaussian curves for each sample synthesized at 100^{o}C to 700^{o}C. The Raman fitted peaks are presented in Figure 4.13

Apart from finding intensity values, the Gaussian fitting exercise also yielded the true measured frequency centres, the broadening or FWHM and the Gaussian's offset. These fittings are illustrated in Figure 4.13. In keeping with Equations 2.41 and 2.50 which have already been shown to fit large and small grain sizes respectively, charts depicting intensity of chosen phonon peak intensities versus the inverse of grain diameter were plotted and linear fitting were done for the Equation 2.41 for bulk WO_3 and Equation 2.50 for nano-WO_3. All calculations performed are summarized in a Table 4.2

This is an experimental evidence of the fact that a plot of intensity of a phonon peak versus the inverse of the grain size of the grains can be estimated to a linear relationship only for

relatively larger grain sizes than about 100 nm as shown in Figure 4.14. On the other hand, a plot of the ratio of ratio of the intensities of the neighboring peaks versus the inverse of the grain size of the grains gives a linear fit at smaller grains than 100 nm as shown in Figure 4.15 and non-linearities are apparent beyond 100 nm as expected.

It has generally been observed from both the theoretical and the experimental results that an inverse relationship is obtained when lower intensities from lower Raman frequency phonons is divided by higher intensities from higher Raman frequency phonons. For instance dividing I_{700} by I_{800} where I_{700} is less than I_{800} yield an inverse relationship with grain diameter d. On the other hand higher intensity from lower Raman frequency phonons divided by lower intensities from higher Raman frequency phonons yields a directly increasing relationship with d. This is clearly confirmed by the polynomial division in Equation 2.47. For small grains the equation suggests that when I_{700} is less than I_{800} then ${}_1\Pi_2$ is almost proportional to $1/d^2$. This is the case where a smaller polynomial is being divided by a bigger one. The reverse process yields the ratio ${}_1\Pi_2$ being proportional to d^2. In the other case where I_{800} is being divided by I_{960} when I_{800} is greater than I_{960} a positively increasing ${}_1\Pi_2$ at a decreasing pace is observed as d is increased. This is probably due to the fact that these ratios may be taken over phonons of differing natures- acoustic or optical phonons.

An important point that is implied in the equation relating ratio of intensities and grain diameter is that, while Equation 2.50 caters for very small grains less that 100 nm in diameter as dictated by the phonon confinement model, Equation 2.41 caters for grains larger than that restriction. Which means Raman spectroscopy may still be used to unveil the size distribution of even moderately larger grains than hitherto allowed. Since these are polynomials dividing each other, new possibilities of evening viewing diameter around phase transition is now possible by evaluating the roots of the denominator so as to determine the asymptotic diameters.

A quick calculation of the parameters contained in the phonon dispersion relation for WO_3 can be done as follows:

1. First from the table of experimental values Table 4.2 a graph of ${}_1\Pi_2$ versus inverse of d^2 is drawn as shown in Figures 4.15. Compare with the traditional approach by

Tuinstra and Koenig .

2. The intercept,C and the slope M are obtained from the graph. These are found from the graph of ratio of 700 and 800 cm-1 phonon intensity versus inverse of d^2 to be (0.90 $\pm$ 0.02) and (1.22 $\pm$ 0.88)$\times$ 10^{-9} respectively.

3. Bearing mind that ω_1=700cm^{-1} and ω_2=800 cm^{-1} and the natural line width, $\Gamma_0 = 8$ cm^{-1} and substituting all this information into Equations 2.56 and 2.58..

These quick calculations yeild an optical branch of dispersion relations of WO_3 given as

$$\omega\left(q\right) = 795.59 \mp 133 sin^2\left(\frac{aq}{4\pi^2}\right) \tag{4.2}$$

or

$$\omega\left(q\right) = 420.88 \pm 108.43 sin^2\left(\frac{aq}{4\pi^2}\right) \tag{4.3}$$

This phonon dispersion equation is with an percentage error of 2.5 per cent. The fact that 804 cm^{-1} is the major vibrational mode in WO_3, the phonon dispersion relation in Equation 5.1 is the most plausible.

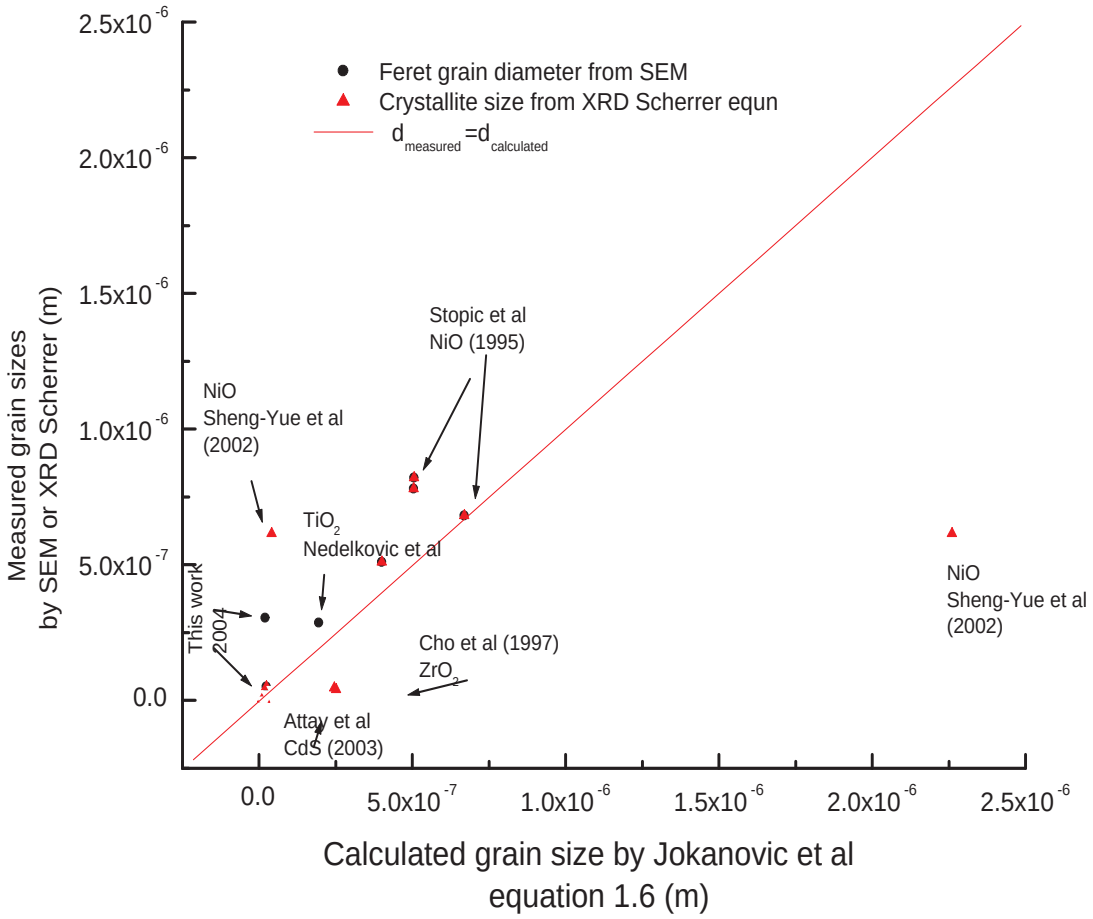

Figure 4.1: Measured grain size compared to calculated grain sizes of various materials from various researchers. Measurements are done using either SEM or Xray diffraction and calculated data are accomplished the Jokanovic model on ultrasonically generated droplets. Present work's calculated and measured data took into account the refinements in the Jokanovic's model presented in Chapter 2

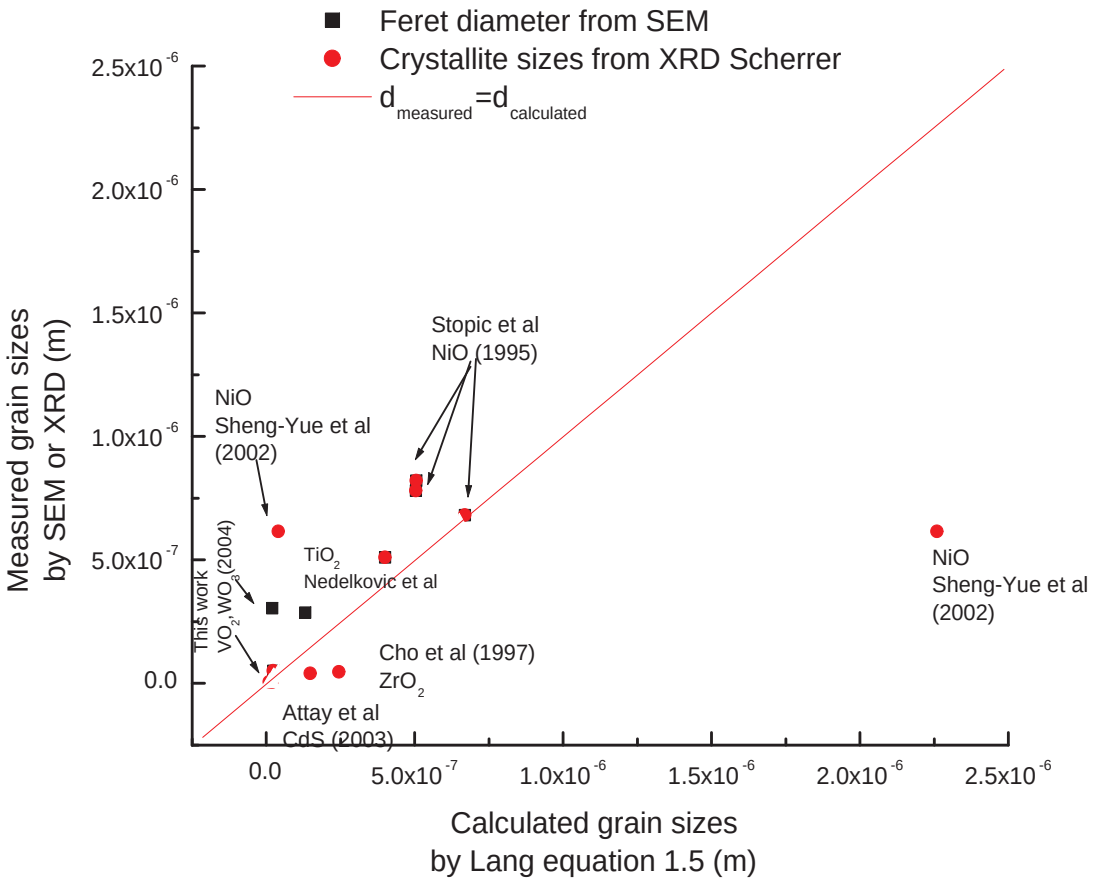

Figure 4.2: Measured grain size compared to calculated grain sizes of various materials from various researchers. Measurements are done using either SEM or Xray diffraction and calculated data are accomplished using Lang or Jokanovic model on ultrasonically generated droplets. Present work's calculated and measured data took into account the refinements in the Lang model presented in Chapter 2

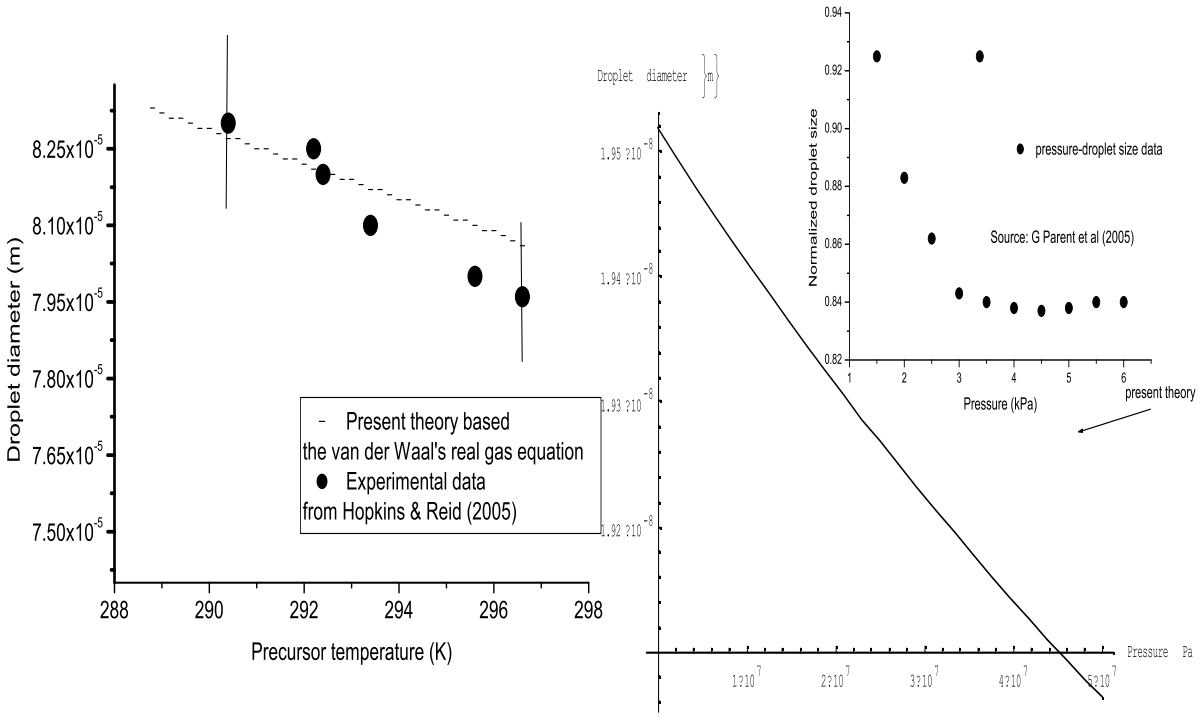

Figure 4.3: Droplets shrink in size as pressure and temperature increase

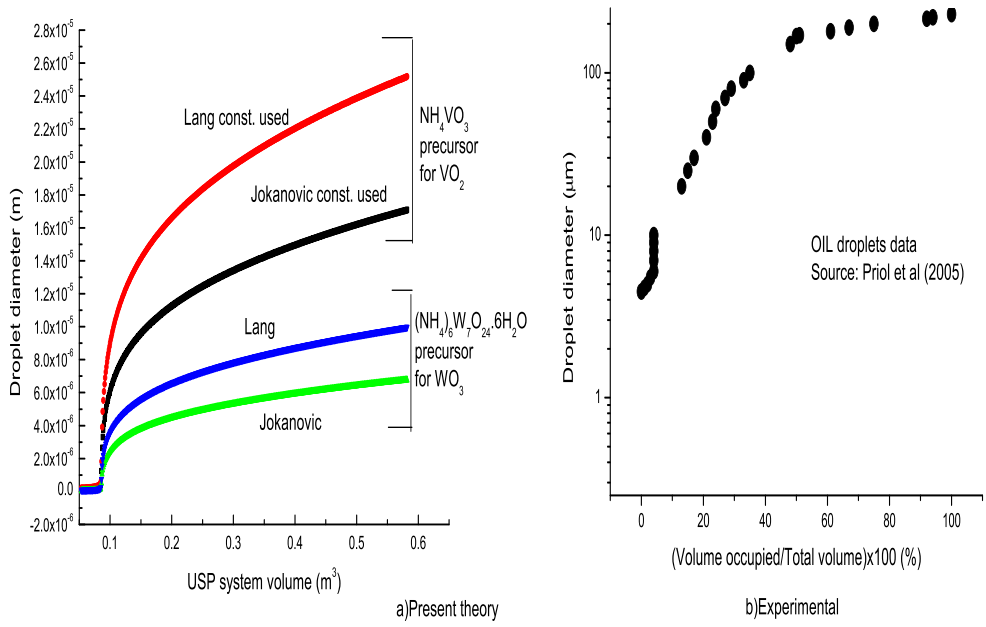

Figure 4.4: Large volume tends to contain large droplet whereas small volume tends to contain small droplets

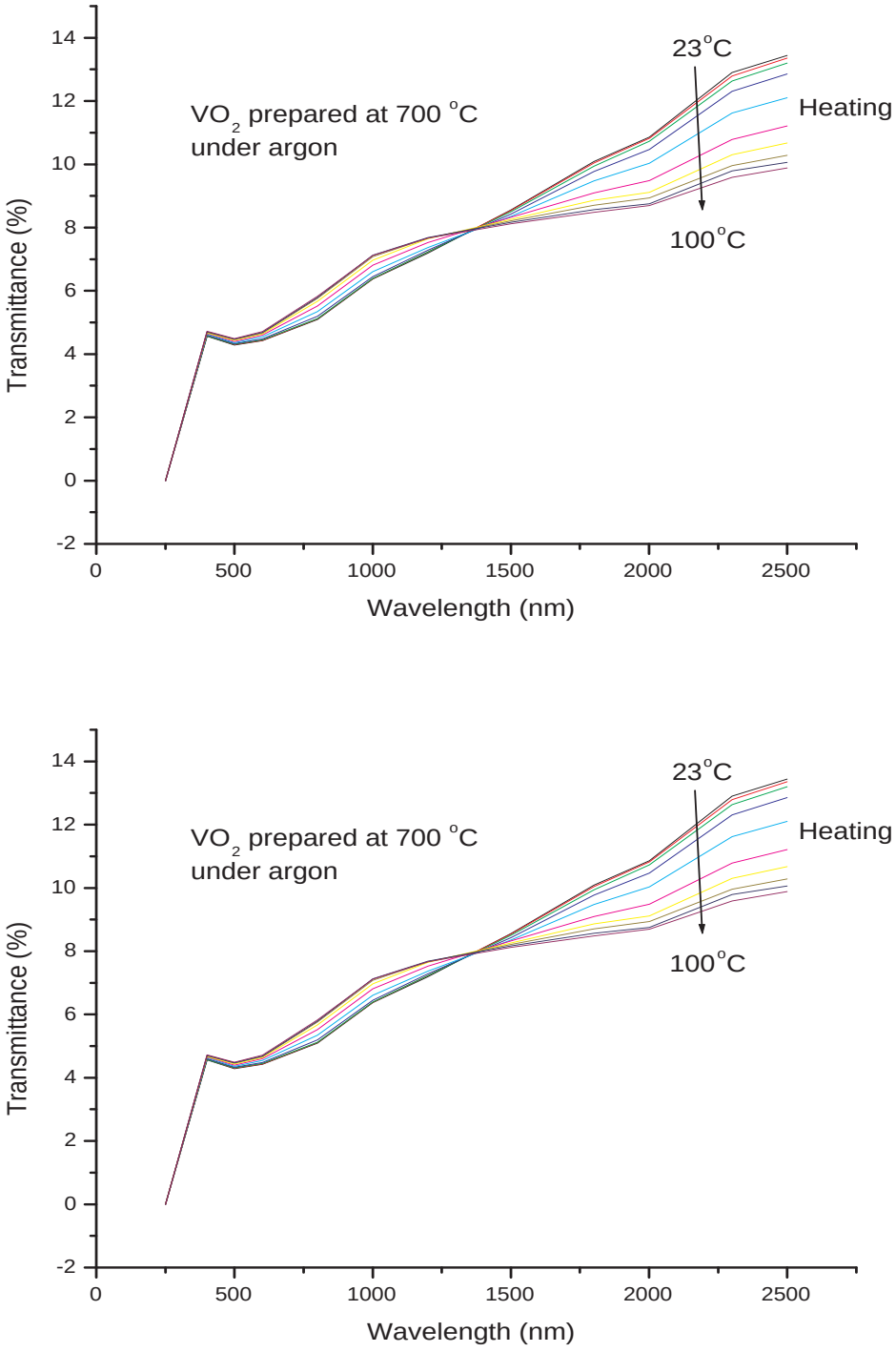

Figure 4.5: Transmittance at different wavelengths in different samples of vanadium oxides synthesized under argon produced from the same precursor as samples in Figure 4.5 but enriched with VCl_3 as illustrated. These were taken at a range of temperatures from room temperature in steps indicated to any temperature above the transition temperature of VO_2 (b) and the cooling the sample back to room temperature(a)

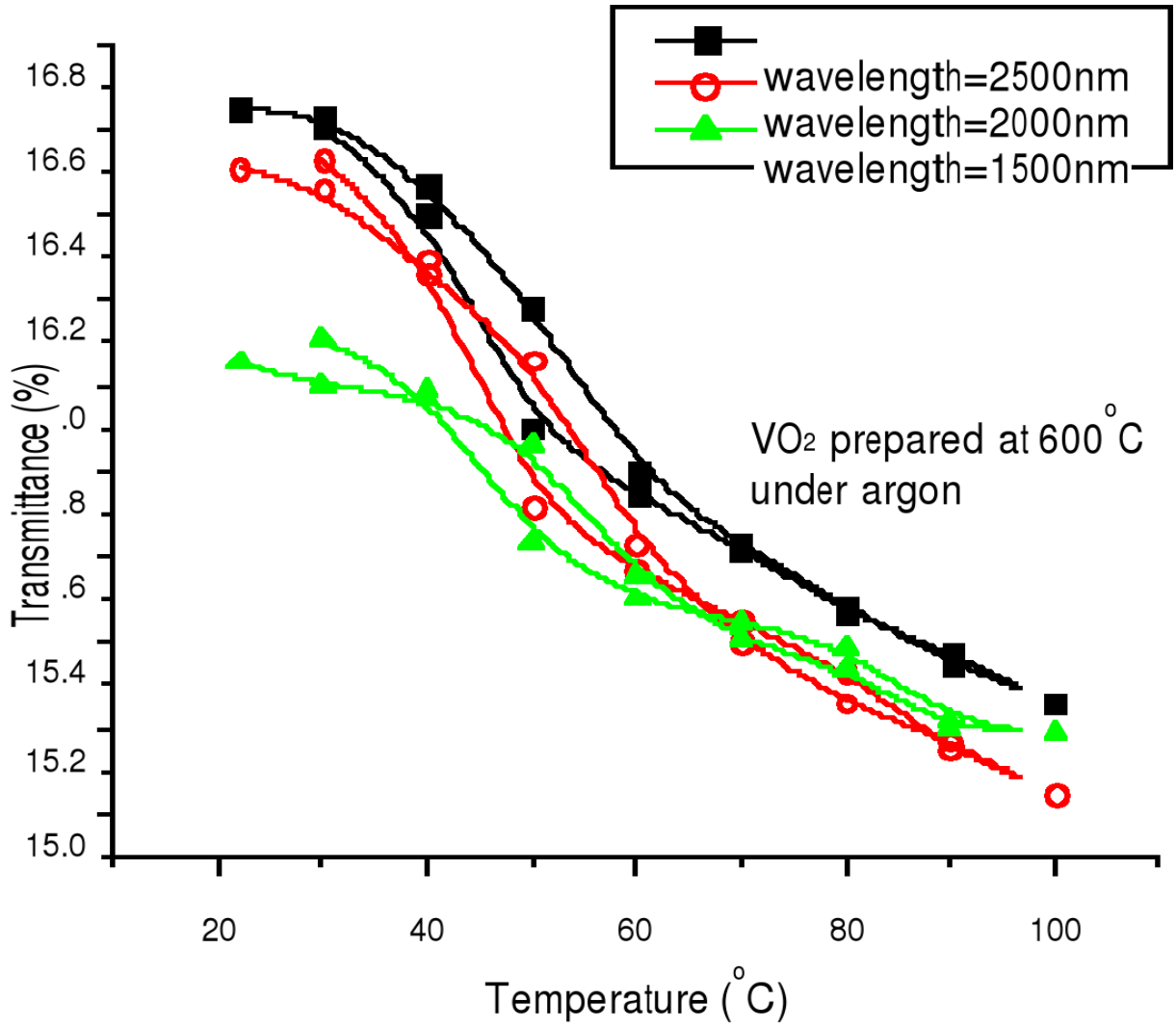

Figure 4.6: Transmittance versus ambient temperature for a sample prepared under argon at 600^{o}C at different wavelength of radiation

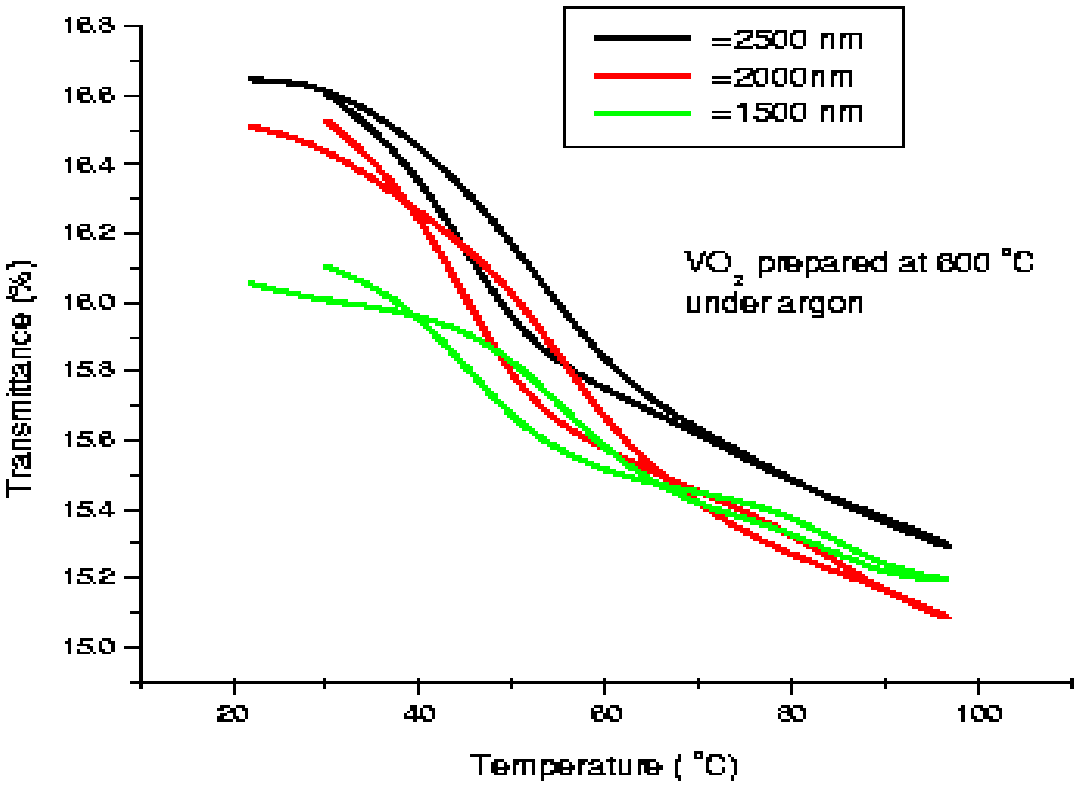

Figure 4.7: Transmittance- ambient temperature hysteresis plots for a sample prepared under argon at 700^{o}C at different wavelengths of incident radiation

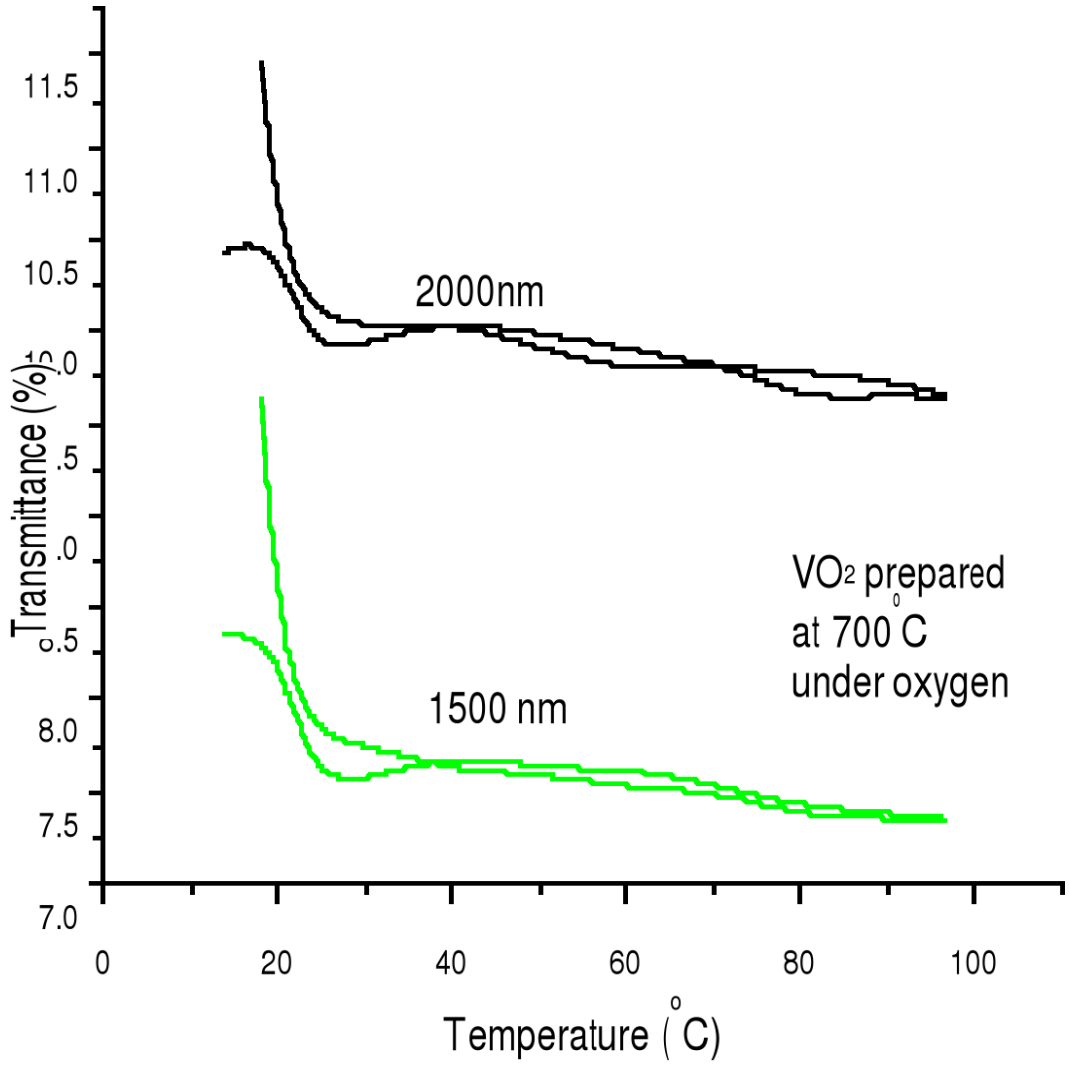

Figure 4.8: Transmittance- ambient temperature hysteresis plots for a sample prepared under oxygen at 700^{o}C at different wavelengths of incident radiation revealing a drastically reduced transition temperature of about 23^{o}C

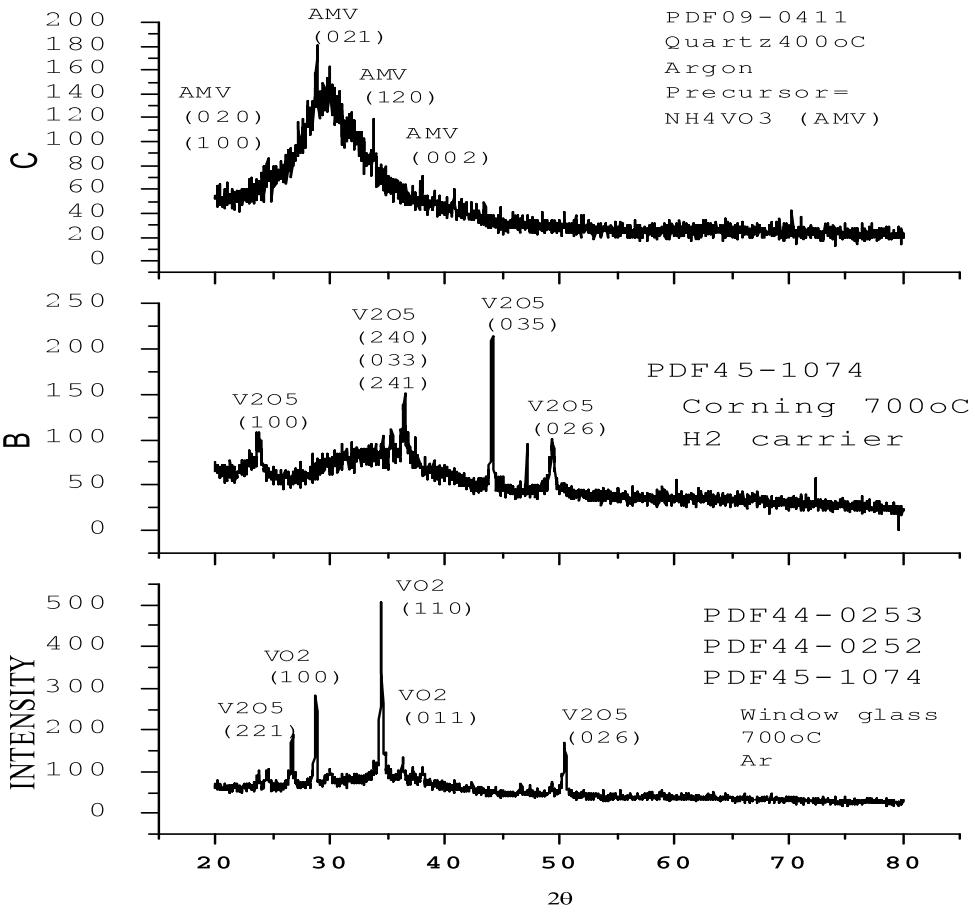

Figure 4.9: X- ray diffraction spectra of samples V1, V8 and V5 in descending order respectively. Note the absence and/or weakness of VO_2 characteristic (100) peak in all the spectra. Other phases of vanadium oxides are obviously present thereby muffling the thermochromic properties of less abundant VO_2

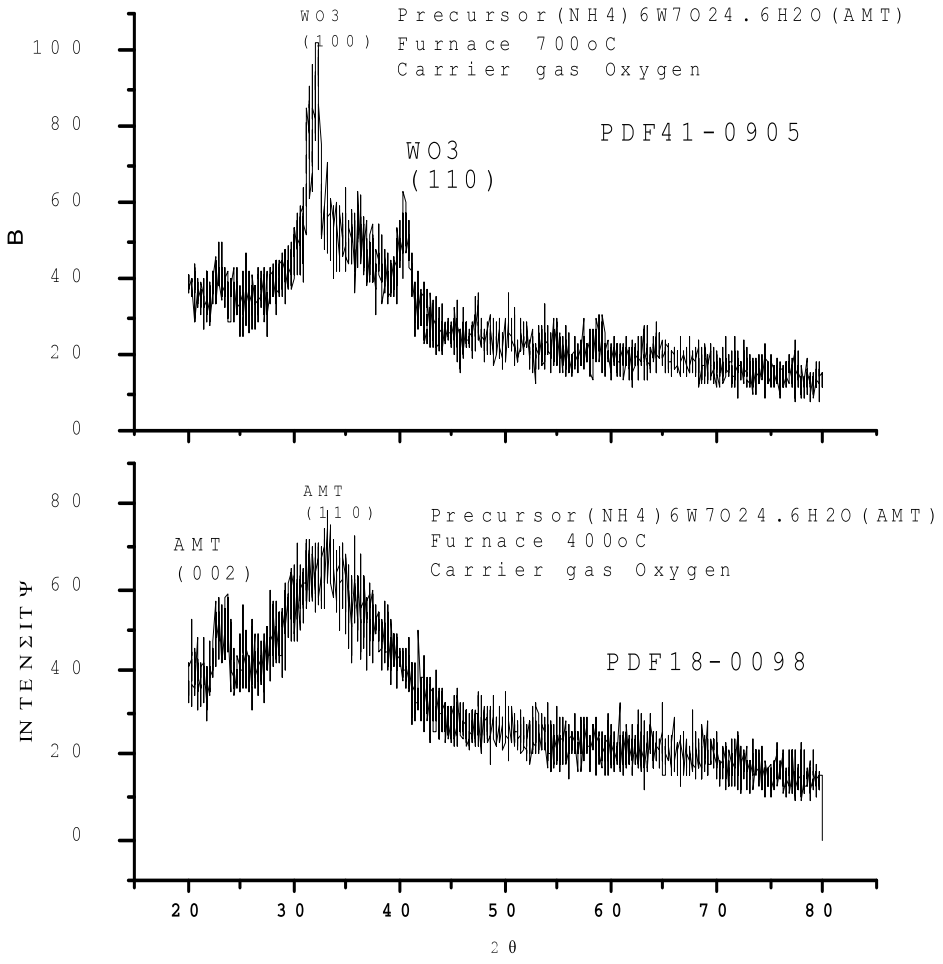

Figure 4.10: X-ray diffraction spectra for WO_3 samples synthesized at 400^{o}C and 700^{o}C showing WO_3 being amorphous at 400^{o}C and crystalline at higher synthesis temperature.

Table 4.1: An outline of previous an present findings of Raman phonon modes in VO_2

Petrov	Schilbe	Aronov	Srivastava and Chase	Vikhnin	Pan	Present	Present	Present
							58	93
							67	
						119	104	
142	149–	149–		144–		141	153	140
191Ag	199Ag	200Ag	208B1g	194Ag	192Ag	204		193
221Ag	225Ag	226Ag	236	226Ag	225Ag			
258Ag	259Bg	259Ag		260Ag	258Ag			
	265Ag				265Bg	264		
308Ag	313Ag	313Ag		311Ag	308Ag	304	307	280
335Ag	339Ag	340Ag		337Ag	339Ag			
392Ag	392Ag	392Ag		389Ag	392Ag			
	395Bg				395Bg			
						424	413	401
	444Bg	436Ag	450E1g	438Ag	44Bg		444	
	453Bg				453Bg			
	489Bg			493Ag	489Bg	484		
497Ag	503Ag	501Ag			503Ag	504	501	513
						564		
594Bg	595Ag	594Bg		595Ag	585Ag			583
612Ag	618Ag	620Ag		615ag	618ag		612	613
			655A1g	627Ag		627		
	670Bg				650Bg	676		684
							693	691
	830Bg				825Bg			
			850B2g					
								995

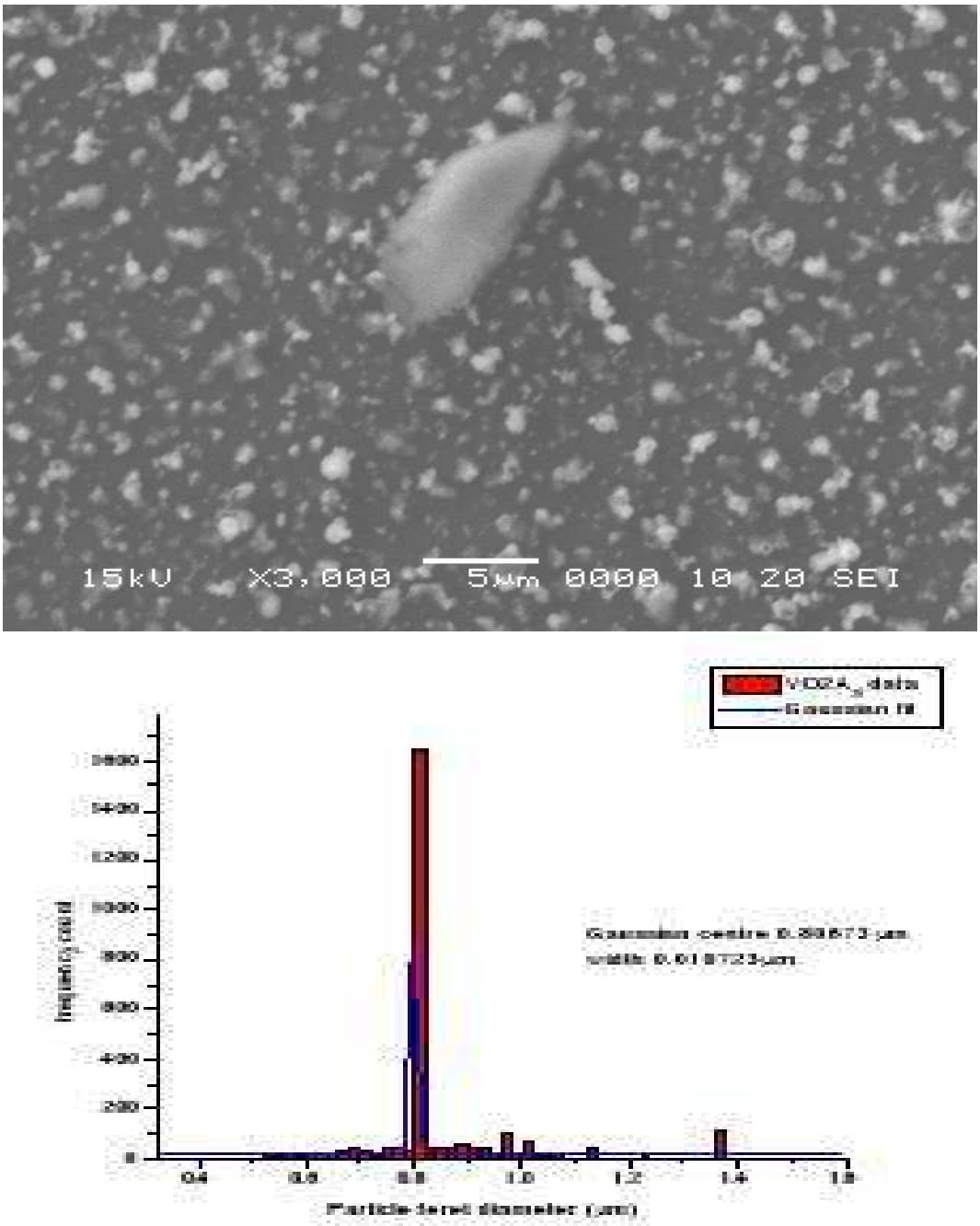

Figure 4.11: Images of VO_2 synthesized at 600^{o}C and their respective frequency distributions of grain area, feret diameter and perimeter for sample V11.

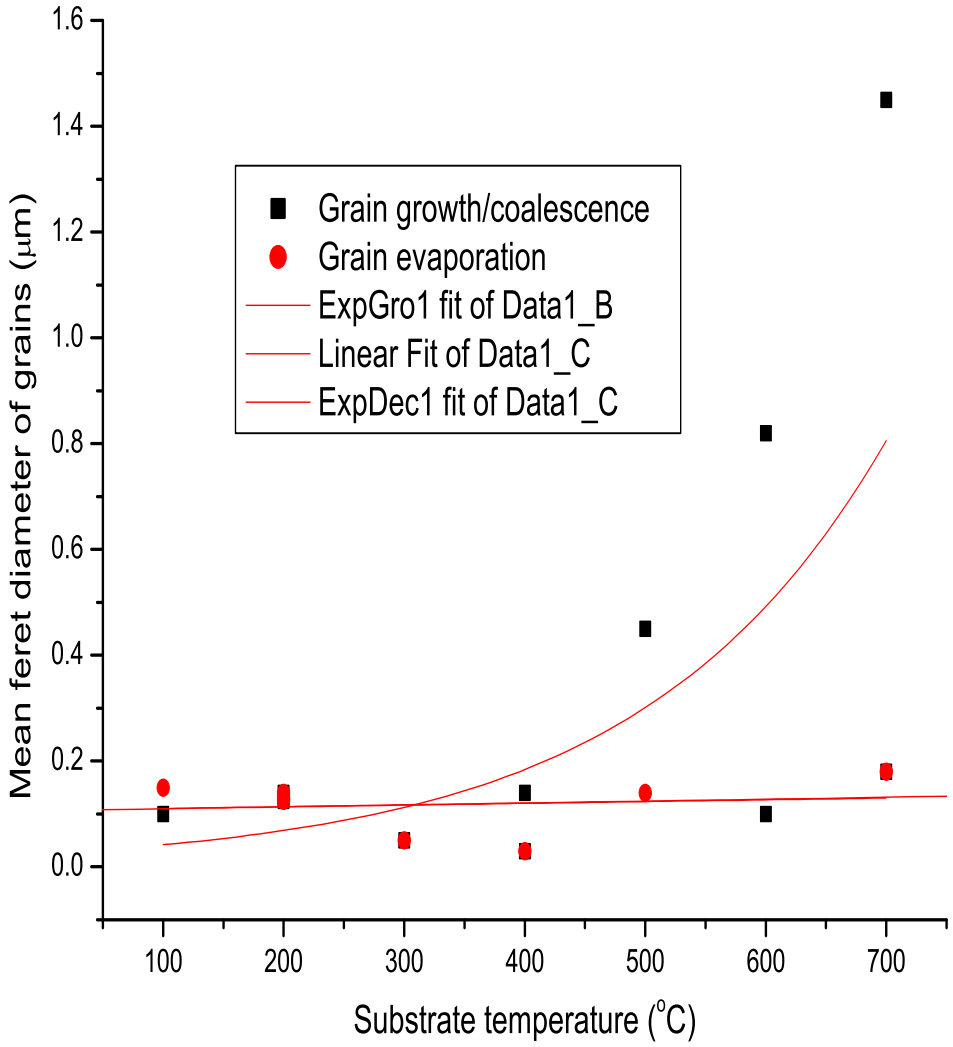

Figure 4.12: A plot of grain diameter against the substrate temperature reveals three possibilities: most of the grains gain size exponentially with substrate temperature due to coalescence of neighboring grains, some remain unchanges while the rest shrink in size due to evaporation of some of the material from the grain

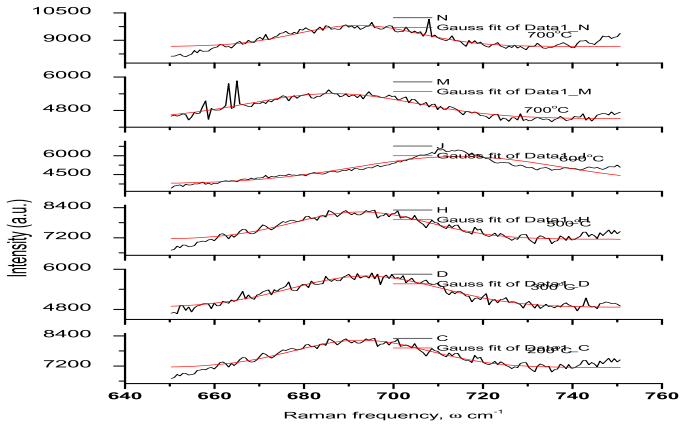

(a)

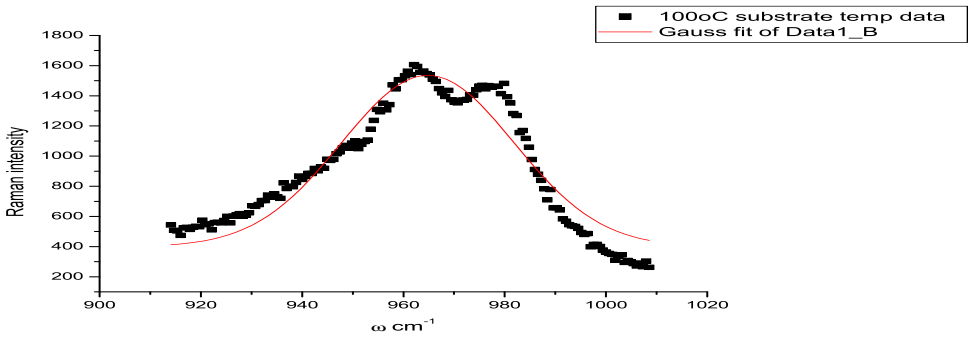

(b)

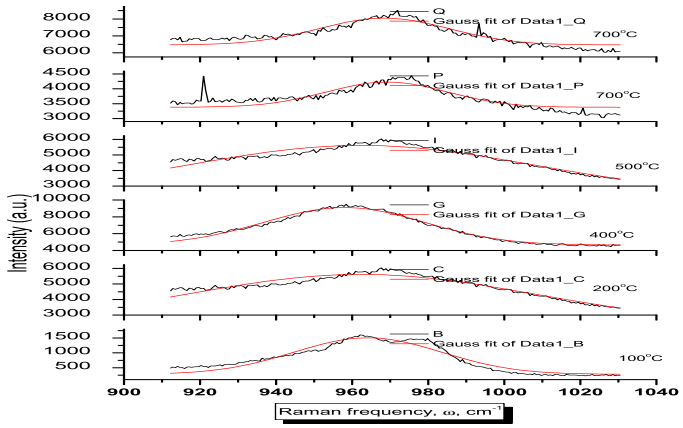

(c)

Figure 4.13: The phonon peaks at Raman frequencies of 700 cm^{-1} (a) and 960 cm^{-1}(c) are each fitted with the Gaussian in order to obtain values of intensity, peak brodening and frequency shifts The same was done for the phonon peak 800 cm^{-1} (not shown). Asymmetric broadening is clear vindicated in (b) and this qualifies for description by the phonon confinement model

Table 4.2: Summary of calculations done and data obtained from Raman spectra of varying nano-sizes of WO_3 for the fitting these data with the linearized PC model of the the present study

Grain diameter, d (nm)	d^{-1}	I(ω_1)	I(ω_2)	I(ω_3)	Ratio $_1\Pi_2$	Ratio $_3\Pi_2$
20	5.00×10^7	3982	4784	9247	0.83	1.93
30	3.33×10^7	1561	1763	5207	0.89	3.21
80	1.25×10^7	266	314	1533	0.85	4.88
150	0.67×10^7	319	383	369	0.83	0.96
150	0.67×10^7	2307	2514	2789	0.92	1.11
150	0.67×10^7	1890	2209	2231	0.86	1.01
170	0.59×10^7	9512	17947	7766	0.53	0.43
250	4.0×10^7	422	453	971	0.93	2.14
550	0.18×10^7	8166	12913	5607	0.63	0.43
840	0.12×10^7	5407	11572	5524	0.47	0.41
1510	0.07×10^7	5317	10978	3887	0.48	0.35

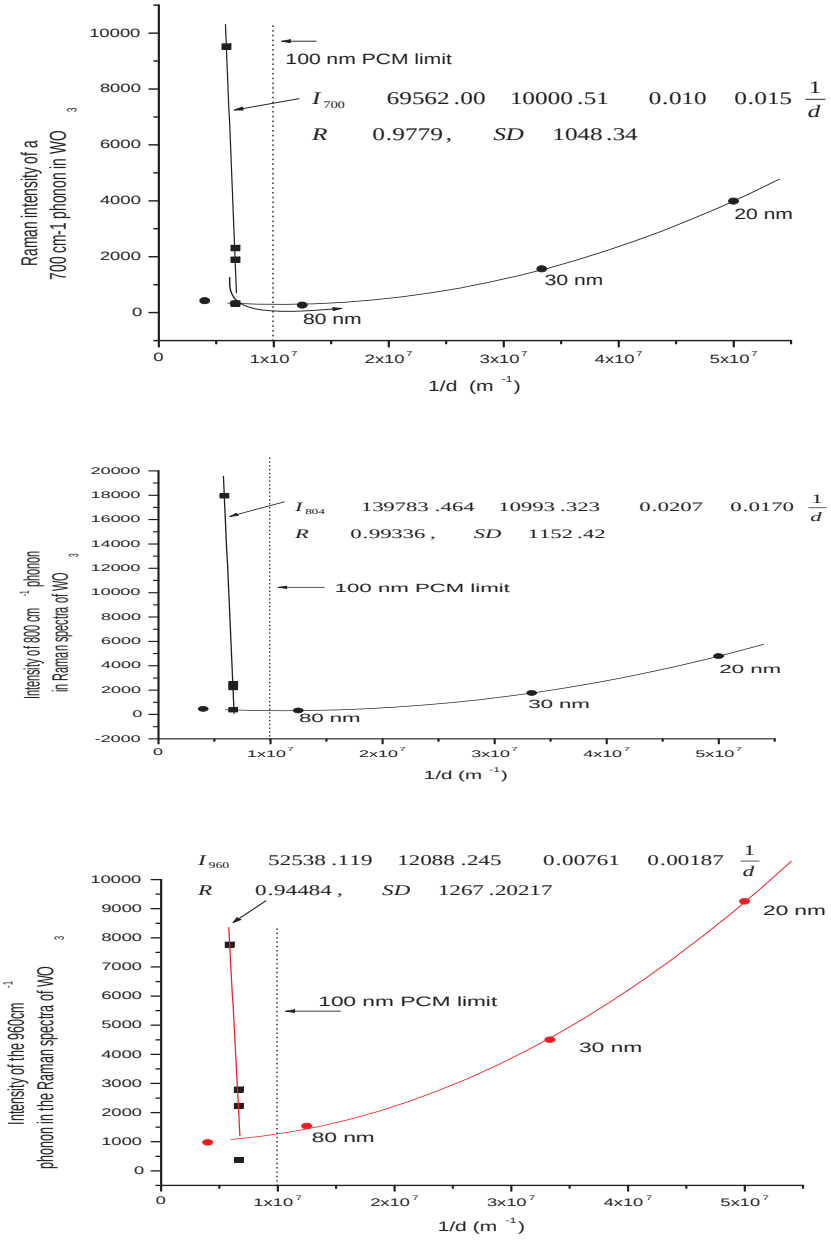

Figure 4.14: A linear nature of these plots of phonon intensities versus inverse of diameter is clearly revealed at larger than 100 nm of d

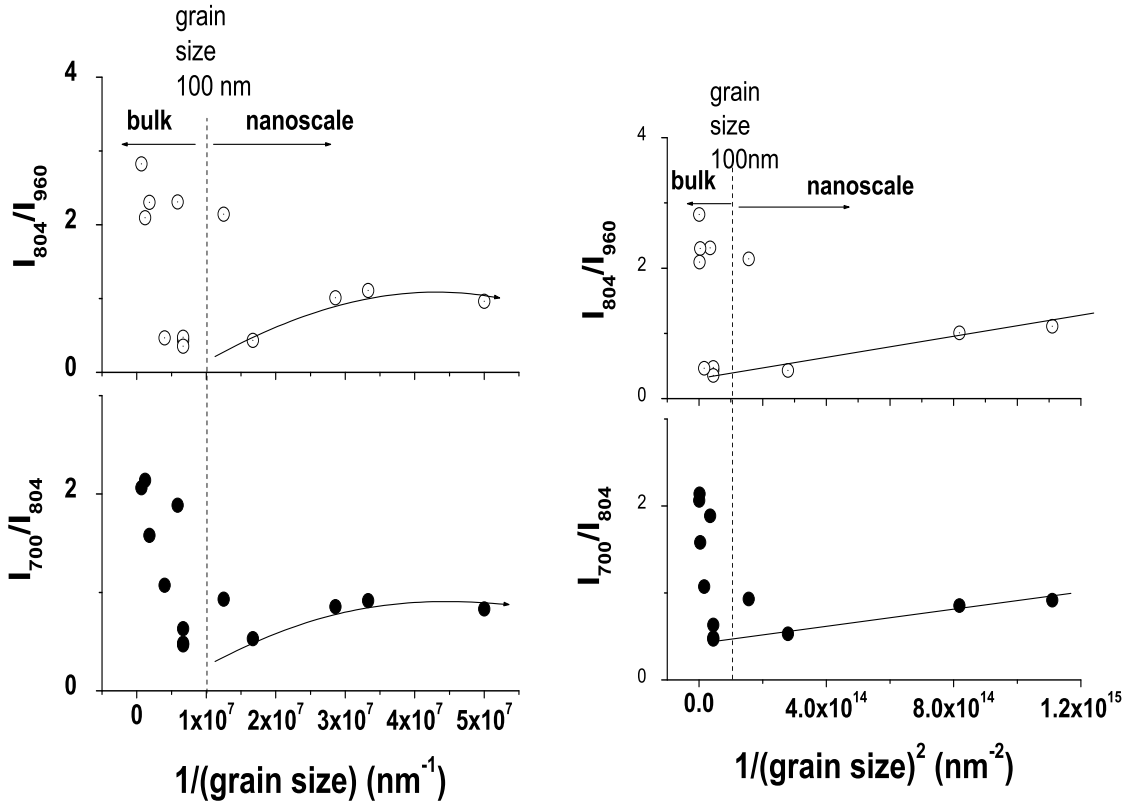

Figure 4.15: For plots of the ratios of phonon intensities of neighbouring peaks versus the inverse of d^2, a cut off point of 100 nm between linear and non-linear fittings is clearly apparent. Note how clearly linear the present plot is as compared to the non-linear one based on the Tuinstra and Koenig equation

Chapter 5

Conclusions

5.1 Diameters of ultrasonic droplets and their resulting deposited grains

Conflict between the theory and experiment with regard to the distribution of the droplet size generated by ultrasonic spray has been presented. The available theories-the Lang model and the modified version of it- the Jokanovic model- have been found to be inadequate in the absence of the dynamic properties of temperature, pressure and the volume that the droplets occupy. In this dissertation, a further modification of both models has been done by considering a temperature dependent surface tension parameter and a p-V-T_{pr} dependent density of the precursor solution and the USP system. To test the validity of the new modification, examples have been given for cases of the ultrasonic spray pyrolysis of vanadium and tungsten oxides. Also, a review of previous attempts to reconcile experiment to theory has been presented. Pressure and precursor temperature affect droplet diameter in a similar manner in that both tend to reduce the droplet size as they are allowed to rise. Temperature contributes to at least 16 per cent loss in diameter as it rises from room to boiling point of water. Pressure however has been found from the present model to reduce the droplet size by about 14 per cent from slightly below atmospheric pressure to about twice the atmospheric pressure. A compunding effect when both temperature and pressure rise can be very substantial translating to about 30 per cent of the droplet diameter being lost before the actual

pyrolysis takes place.

In the present study, with this evidence at hand, it can be concluded that those previous researchers that have found their calculated grain sizes (using the uncorrected Lang or Jokanovic model) to be larger than the measured, it is because the temperature and pressure effects are not considered during calculation. Inclusion of these effects would bring the calculated grain size down to the regions of the measured grain.

Volume occupied by droplets or volume of the USP system, as another thermodynamic variable that was considered in the present study, has surprisingly shown to be much more critical to the droplet size than pressure and temperature. Droplet size blow up so rapidly when they have to occupy large volumes with the reverse being true. A rather radical conclusion that small USP systems would be suited for generating nanometric material, the present study has found enough compelling experimental evidence to prove that when droplets are confined in a small volume they tend to retain their small sizes. It has been shown that Priol et al (2005)[91] when studying the effect of shape and size of electrostatic injectors, did find that smaller injectors produce more highly charged droplets that were not only small in size but tended to occupy small volume. The present study has also experimental evidence from laser pyrolysis where the aerosol to be pyrolysed by the laser is carried through a co-axially flowing argon jet-with the aerosol droplets at the axis of the argon "pipe"- a practice that not only prevents the pyrolysol from contacting the wall of the chamber thereby contaminating the so-produced materials but also prevents spread of the particles which may lead to broadening of the size distribution due to volume effects.

It can be recommended that when calculating droplet and grain sizes using either Jokanovic or Langs model, it is important to include the thermodynamic state of the droplet in the calculation. Often, the ultrasound generator raises the temperature of the starting solution so continuously that during the entire period of synthesis process the precursor temperature is never constant. This contributes to the wide distribution of grain sizes. The volume of the USP system, however, would not be a problem since this only varies from the design of the USP system to the other. An important note on volume as a variable is that during design of the USP system, confinement of the droplet carrying system is highly recommend for the attainment of nanometric materials. Should one intend to synthesize very small particles,

then the dimensions of the USP system should be as small as possible.

It was found in this study that any declared departures of theory from experiment with regard to material grains obtained by ultrasonic pyrolysis is not necessary evidence of the weakness of the theoretical model alone, but rather, the fact that as the droplets condense into grains on a hot substrate, they not only decompose and undergo chemical transformation but also may find chance to coalesce and form bigger particles or undergo evaporation to form smaller particles. These phenomena have to be taken into account when comparing theory with experiment in this regard.

5.2 First synthesis of VO_2 by ultrasonic nebula-spray pyrolysis

Vanadium dioxide is difficult to obtain because of the fact that it is the most unstable of all vanadium oxide phases. This dissertation has presented, in particular, the synthesis of VO_2 by ultrasonic nebula-spray pyrolysis for the first time. A precursor solution of ammonium metavanadate enriched with vanadium tri-chloride was found to be the starting solution from which droplets were generated by an ultrasonic generator operated at 1.7 MHz. The optimum condition for obtaining VO_2, which apply to WO_3 as well, have been presented. X-ray characterization showed the crystals with randomized rather than preferential ordering of the crystal faces. Raman spectra of these materials confirmed the VO_2 signatures obtained from previous findings. The size distribution by scanning electron microscopy showed preferential spherical grains with a modal feret diameter of about 800 nm and mean diameter of 500 nm. Infrared switching confirmed the VO_2 transition temperature in the neighborhood of 60^oC for samples prepared under argon and a drastic shift to room temperature for those prepared under oxygen. Influence of oxygen content in the behavior of such samples was suspected.

5.3 Size controlled synthesis of WO_3 and the determination of its phonon dispersion relations by the present linearization of the phonon confinement model

The fact that WO_3 grains obtained by UNSP generally gain size in an exponential growth as the substrate temperature is increased has been elaborated and experimental evidence from this study shown. Raman spectroscopy has been wielded to unveil the size distribution variation as the substrate temperature changes. Based on the phonon confinement model first proposed by Richter et al [1] Faucet and Campbell in 1988[2], this study has accomplished a number of tasks. One of the tasks is the quantification of the empirical suggestion by Kubo et al [87] that cluster size can be correlated to ratio of neighboring peak intensities. From this analysis, a new semi-empirical method has been quantified for the first time which has been hitherto been used to predicting the size distribution of grains in a sample simply by relating a characteristic Raman peak intensity to the inverse of the grain mean diameter. In agreement with previous practice, the so derived Equation 2.43 suggests that large particle diameters have a very small contribution to phonon intensities; which means that, as a means of simplification, this equation can, by neglecting high terms, be used to linearize the intensity-vs-inverse of diameter charts. This kind of analysis has radically shown, in contrast to conventional belief and practice, that intensity-versus-crystallite-diameter-inverse is only good for bulk state rather that nanometric state.

Pursuing the ratio of intensities of neighboring Raman peak in a spectrum has earned this present study another important information. The restriction of the phonon confinement model in the range 0 to 100nm is completely vindicated the linear in the present the Equation 2.50 which suggests that the ratio of intensities for neighboring peaks is more affected by smaller grain diameter than larger ones. A linear plot of this equation has confirmed in a completely new way that the phonon confinement model is indeed suitable for grains in the range 0 to 100 nm provided the the grain diameter values where these ratios of intensities is undefined are taken into account. These may be used to explain the phase transitions in materials in general.

Interestingly, the present linearization of the phonon confinement model has shown that:

1. Knowing the phonon dispersion relations of a material very well and having the Raman spectra of heterogeneous samples of a material, it is easy to predict the size distribution of the grains on the material as has been the practice.

2. Having Raman spectra of a material with varying grain sizes and if the grain sizes are very well know, it is possible to work out the phonon dispersion relations of that material. This is done simply by plotting a graph of ratio of neighboring peak intensities against the inverse of d and obtaining the slope and intercept of the graph which are in turn used to calculated the parameters contained in the phonon dispersion relation of such a material. This is good news for materials that cannot be analyzed for their phonon dispersion relations using neutron scattering.

3. Only ratio of intensities of neighboring peaks (and not simply intensity of peaks) yields the full information about these phonon dispersion relations

A case study for size controlled WO_3 has shown for the first time that this material has a phonon dispersion relations of the form

$$\omega\left(q\right) = 795.59 \mp 133 sin^2\left(\frac{aq}{4\pi^2}\right) \tag{5.1}$$

Whether the ratio of intensities of neighboring peaks versus d^{-2} is inverse or direct was explained as owing to the nature of the phonons from which the intensities are obtained. Acoustic and optical phonon intensities will have varying correlations for acoustic- acoustic, acoustic-optical or optical to optical comparisons.

Bibliography

[1] H Richter, Z P Wang, L Ley, Solid State Commun. 39(1981)625

[2] P M Faucet, I H Campbell, Critical Rev. Solid State Mater. Sci. 14 (1988) 79

[3] D R dos Santos and I L Toriani, Solid State Commun. 85(1993) 307

[4] C Bittencourt R Landers E Llobet, X Correig and J Calderer, Semicond. Sc. & Technol. IOP,17 No 6 (2002) 522-525

[5] S H Wang, T C Chou and C C Liu, Sensors and Actuators B 94 (2003) 343-351.

[6] V Guidi, M Blo, M A Butturi, M C Carotta, S Galliera, A Giberti, C Malagu, G Martinelli, M Piga, M Sacerdoti and B Vendemiati, Sensors and Actuators B 100 (2004)277-282

[7] P Ivanov, J Hubalek, K Malysz, J Prasek, X Vilanova, E Llobet, X Corrieg, Sensors and Actuators B 100 (2004)293-297

[8] M Bendahan R Boulmani, J L Seguin, K Aguir,Sensors and Actuators B100(2004)320-324

[9] A Hoel, L F Reyes, P Heszler, V Lantto CG Granqvist, Current Applied Physics 4 (2004) 547-553

[10] H Kawasaki, J Namba, K Iwatsuji, Y Suda, K Wada, K Ebihara, T Ohshima, Appl. Surface Science 197-198 (2002) 547-551

[11] same as [6]

[12] A H Jayatissa, S T Cheng, T G, Materials Science and Engineering B 109 (2004)269-275

[13] H Kamal, A A Akl, K Abdel-Hady, Physica B 349 (2005) 192-205

[14] S Djerad L Tifouti, M Crocoll W Wesweiler, Journal of Molecular Catalysis A: Chemical 208 (2004) 257-265.

[15] Q Sun, B K Rao, P Jena, D Stolcic, G Gantefor, Y Kawazoe, Chemical Physics Letters 387 (2004) 29-34.

[16] G Leftheriotis, S Papaefthimiou, P Tianoulis, A Siokou, D Kefalas, Applied Surface Science 218 (2003) 275-280.

[17] J Shieh, H M Feng, M H Hon, H Y Juang, Sensors and Actuators B86 (2002) 75-80.

[18] M Ando, R Chabicovsky, M Haruta, Sensors and Actuators B 76 (2001) 13-17.

[19] P R Patil, P S Patil, Thin Solid Films 382 (2001) 13-22.

[20] P S Patil, S B Nikam, L D Kadam, Materials Chemistry and Physics 69 (2001) 77-83.

[21] J Arakaki, R Reyes M Horn, W Estrada, Solar Energy Materials and Solar Cells 37 (1995) 33-41.

[22] S Capanoe, R Rella, P Siciliano, L Vasanelli,Thin Solid Films 350 (1999) 264-268.

[23] M I Baraton, L Merhari, H Ferkel, J F Castagnet, Materials Science and Engineering C 19 (2002) 315-321.

[24] I Levkowitz, M Dowell and M A J Shields, Solid State Chem. 15 (1975) 21-39.

[25] C N R Rao and G V S Rao, Natl. Stand. Ref. Data Ser. Natl Bur. Stand 49 (1974) 117-122.

[26] K L Kehl,R G Hay, and D Wahl (1952) J. Appl.Phys, 23, 212-215.

[27] E Salje, Acta Cryst. B33 (1977) 574-577

[28] S Tanisaki, J.Phys. Soc. Jpn 15 (1960) 573-581

[29] B O Loopstra and P Boldrini, Acta Cryst. B25 (1966) 158-162.

[30] B O Loopstra and H M Rietveld, Acta Cryst. B25 (1969) 1420- 1421.

[31] Z Braekken, Z. Kristallogr. 78 (1931) 484-488.

[32] S Tanisaki, J. Phys. Soc. Jpn (1960) 573-581.

[33] E Salje, Ferroelectrics 12 (1976) 215-217.

[34] S Tanisaki, J. Phys. Soc. Jpn (1960) 566-573.

[35] R Diehl and G Brandt, Acta Cryst. B34 (1978) 1105- 1111.

[36] C G Grangvist, E Avendano, A Azens, Thin Solid Films 442 (2003) 201-211.

[37] N. F. Mott, Reviews of Modern Physics, 1968; 40(4): 677

[38] F. J. Morin, Phys; Rev. Lett., 1959; 3: 34

[39] D. Adler, Reviews of Modern Physics, 1968; 40(4): 714

[40] F. J. Morin, Phys; Rev. Lett., 1959; 3: 34

[41] Vibrational spectroscopy of phase transitions, edited by Z. Iqbal and F J Owens (Academic, Orlando, FL, 1984) pp 312-318

[42] J B Goodenough, J. Solid State Chem. 3 (1971) 490.

[43] S Shin, S Suga, M Tanuguchi, M Fijisawa, H. Kansaki, A Fujimori, H Damon, Y Ueda, K Kosuge, and S Kachi, Phys. Rev. B41 (1990) 4993

[44] D Paquet, and P Leroux-Hugon, Phys. Rev. B22 (1980) 5284

[45] J. C. Lee, G. V. Jorgenson and R. J. Lin, Proc. SPIE 1986; 692: 2

[46] P. Jin, M. Tazawa, T. Miki, and S. Tanemura, The 3rd IUMRS-ICAM (Int. Conf. On Advanced Materials) Aug. 31- 4 Sept., Tokyo, (Paper No. KP 57 in Ecomaterial session) 1993

[47] S. M. Babulanam, T. S. Eriksson, G. A. Niklasson and C. G. Granqvist, Solar Energy Mat. 1987; 16 (5): 347-363. K. Kuwabara, S. Ichikawa, and K. Sugiyama, J. Electrochem. Soc. 1988; 135, 2432

[48] W. R. Roach, Appl. Phys. Lett. 19 (1971) 453

[49] A. W. Smith, Appl. Phys. Lett. 23 (1973) 437

[50] D. D. Eden, Opt. Eng. 20 (1981) 337

[51] M. Fukuma, S. Zembutsu and S. Miyazawa, Appl. Opt. 22(2) (1983)265-268

[52] M. F. Becker, A. B. Buckman, R. M. Walser, T. line, P. Georges, and A. Brun, Appl. Phys. Lett. 1994; 65 (12): 1507-1509

[53] G. Guzman, F. Beteille, R. Morineau, and J. Livage, J. Mat. Chem. 6 (1996) 505-506

[54] R Diehl and G Brandt, Acta Cryst. B34 (1978) 1105-1111

[55] Z P Wuyx, S Yamamotoy, A Miyashitay, Z J Zhangz, K Narumiz and H Naramotoz, J. Phys.: Condens. Matter 10 (1998) L765-L771

[56] Futaki H and Aoki M 1969 Japan. J. Appl. Phys. 8 1008

[57] Semonov A L 1994 Phys. Solid State 36 1079

[58] F C Case, J. Vac. Sci. Technol. A5 (1987) 1762

[59] L A Gea and L A Boatner, Appl. Phys. Lett. 68 (1996) 3081

[60] P J Hood and J F DeNatale, J. Appl. Phys. 70 (1991) 176

[61] R.J. Lang, J. Acoust. Soc. Am., 34 (1962) 6.

[62] V. Jokanovic, Dj Janackovic, A. Spasic, D. Uskokovic, Mat. Trans. JIM., 37 (1996) 626.

[63] S Y Cho, I T Kim, D Y Kim, S J Park, B K Kim, J H Lee, Mat. Letts. 32 (1997) 271-273.

[64] Y C Chang, S B Park, S W Kwon, J. Colloid and Interface Sci. 182 (1996) 59- 62.

[65] A K Ivanov-Schitz, A V Nistuk, L N Demianets, N G Chaban, Solid State Ionics 144 (2001) 133-141.

[66] M Langlet, E Senet, J L Deschanvres, G Delabouglise, F Weiss, J C Joubert, Thin Film Solids 174 (1989) 263.

[67] T Setoguchi, M Sawano, K Eguchi, H Arai, Solid State Ionics 40/41 (1990) 502

[68] Y Saito, O. Nakamura, Y. Yamamoto. J Mater. Sci. 29 (1994) 4713

[69] C S Hong , P Ravindranathan, DK Agrawal, R Roy, J Mater. Sci. Lett. 13 (1994) 1015

[70] H Kamiya, H Suzuki, D Kato, G Jimbo, J. Am. Ceram. Soc. 76 (1993) 54

[71] A. Furusaki, H. Konno, R. Furuchi, J. Mater. Sci. 30 (1995) 2829.

[72] C S Huang, C S Tao, C H Lee, J.Electrochem. Soc. 10 (1997) 3556

[73] Y. Matsuzaki, M. Hishinuma, I. Yasuda, Thin solid Films 340 (1999) 72-76.

[74] H Huang, E M Kelder, L. Chen, J. Schoonman, Solid State Ionics 120 (1999) 205- 210.

[75] E. Djurado, E. Meunier, J. Solid State Chem. 141 (1998) 191 (see also 48)

[76] A R Raju, H N Aiyer and C N R Rao, Solid-Solid Interfaces (1997) pp70-88.

[77] A R Raju and C N R Rao, App.Phys.Lett 66 (7) (1995) 896-898.

[78] M Langlet, J C Joubert, In Chemistry of Advanced Materials, ed. C N R Rao, IUPAC, 21st Century Monogr.Ser., Blackwell, Oxford, 1993.

[79] P Murugavel, S Kalaiselvam, A R Raju and C N R Rao, J. Mater. Chem. 7(8) (1997) 1433-1438

[80] F G L Rothchild J Sloan, A Rosentsveig, R Popovitz-Biro and R J Tenne, J. Solid State Chem. 162 (2001) 300-314

[81] G A De Wijs, R A de Groot, Electrochimica Acta 46 (2001) 1989- 1993

[82] J Grabrusenoks, A Veispals, A von Czarnowski, K H Meiwes-Broer Electrochimica Acta 46 (2001) 2229- 2231.

[83] O Pyper, A Kaschner, C Thomsen, Solar Energy Mat.& Solar Cells 71 (2002) 511- 522

[84] S H Lee, H M Cheong, C E Tracy, A Mascarenhas, D K Benson, S K Deb, Electrochimica Acta 44 (1999) 3111-3115.

[85] M Boulova and G Lucazeau, J. Solid State Chem. 167 (2002) 425-434.

[86] U Serincam G Kartopu, A Guennes, T G Finstad, R Turan Y Ekinci and S C Bayliss, Semicond. Sci.& Technol., 19 (2004) 247-251.

[87] T Kubo and Y Nishikitani, J. Electrochem. Soc, 145 (1998) 1729-1733

[88] P G Abramof, N G Ferreira, A F Beloto, A Y Veta, J. Nanocrystalline Solids, 338-340 (2004) 139-142

[89] G. Parent, J. Momentum. Transfer, 23 (2005) 254-260

[90] R. Hopkins, J. Reid, J. Phys. Chem. A 109 (2005) 7923-7931

[91] L Priol, P Baudel, C Louste, H Romat, J. Electrostatics, 63 (2005) 899-904

[92] M Ivanda, S Music, M Gotic, A Turkovic, A M Tonejc, O Gamulin, J. Molecular Structure, 480-481 (1999) 641-644.

[93] S W Oh, S H Park, C W Park and Y K Sun, Solid State Ionics, In Press, Corrected Proof, Available online 25 May 2004,

[94] K. Matsuda and I. Taniguchi, Journal of Power Sources 132(2004) 156-160

[95] N Khare , D P Singh , H K Singh, A K Gupta, P K Siwach and O N Srivastava, J. Phys. and Chem. Solids 65 (2004) 867-870

[96] J M Bian , X M Li , T L Chen , X D Gao and W D Yu, Applied Surf. Sci. 228 (2004) 297-301

[97] J H Lee and B O Park, Mat. Sc. & Eng. B 106 (2004) 242-245

[98] S H Park, C S Yoon, S G Kang, H S Kim, S I Moon and Y K Sun, Electrochimica Acta 49 (2004) 557-563

[99] Z V Marinkovi, L Mani, J F Cribier, S Ohara, T Fukui and O Miloevi, Mat. Sc. & Eng. A, (2004)

[100] Z V Marinkovi, L Mani and O Miloevi, J. Eur. Ceram. Soc. 24 (2004) 1929-1933

[101] Mihaela Girtan, Surface and Coatings Technology, In Press, Corrected Proof, Available online 31 December 2003

[102] S Y Wang, W Wang and Z H Lu, Mat. Sc. & Eng. B103 (2003) 184-188

[103] F Atay, V Bilgin, I Akyuz and S Kose, Mat. Sc. Semicond. Processing, 6 (2003) 197-203

[104] M Girtan and G Folcher, Surf. & Coatings Technology 172 (2003) 242-250

[105] F Atay, S Kose, V Bilgin and I Akyuz, Mat. Letts. 57(2003) 3461-3472

[106] M Garca-Hiplito, C D Hernndez-Prez, O Alvarez-Fregoso, E Martnez, J Guzmn-Mendoza and C Falcony, Optical Materials 22 (2003) 345-351

[107] M Liu, M L Zhou, L H Zhai, D M Liu, X Gao and W Liu, Physica C: Supercond. 386 (2003) 366-369

[108] S Y Wang and Z H Lu, Mat. Chem. & Phys. 78 (2003) 542-545

[109] K T Wojciechowski and J Obkowski, Solid State Ionics 157 (2003) 341-347

[110] L Castaeda, J C Alonso, A Ortiz, E Andrade, J M Saniger and J G Bauelos, Mat. Chem. & Phys. 77 (2003) 938-944

[111] Y C Kang, H S Roh, H D Park and S B Park, Ceram. Int. 29 (2003) 41-47

[112] D Wang, Smart Mat. Bull., 12(9) (2002),13

[113] A. Ferreri, A. Berenov, Y. Bugoslavsky, G. Perkins and J. L. MacManus-Driscoll, Physica C: Supercond. 372-376 (2002) 873-875

[114] S. Phok, Ph. Galez, J. L. Jorda, Z. Supardi, D. De Barros, P. Odier, A. Sin and F. Weiss, Physica C: Supercond. 372-376 (2002) 876-879

[115] I. Taniguchi, D. Song and M. Wakihara, J. Power Sources, 109 (2002) 333-339

[116] M Dj Blei, Z V Aponji, J M Nedeljkovi and D P Uskokovi, Mat Letts. 54 (2002) 298-302

[117] T Y Ma and D K Shim, Thin Solid Films, 410, (2002) 8-13

[118] SY Wang, W Wang, W Z Wang and Y W Du, Mat. Sc. & Eng. B 90 (2002) 133-137

[119] S Y Wang and Y W Du, J. Crystal Growth 236 (2002) 627-634

[120] I Taniguchi, C K Lim, D Song and M Wakihara, Solid State Ionics 146 (2002) 239-247

[121] K H Kim, J K Park, C H Kim, H D Park, H Chang and S Y Choi, Ceram. Int. 28 (2002) 29-36

[122] A Huanosta, J C Alonso and A Ortiz, Thin Solid Films 401 (2001) 284-290

[123] A K Ivanov-Schitz, A V Nistuk, L N Demianets and N G Chaban, Solid State Ionics 144 (2001) 133-141

[124] A Ferreri, J A G Nelstrop, A D Caplin and J L MacManus-Driscoll, Physica C: Supercond. 351 (2001) 58-61

[125] P Veluchamy, M Tsuji, T Nishio, T Aramoto, H Higuchi, S Kumazawa, S Shibutani, J Nakajima, T Arita, H Ohyama, Solar Energy Mat. & Solar Cells 67 (2001) 179-185

[126] A K Ivanov-Schitz, A V Nistuk and N G Chaban, Solid State Ionics 139 (2001) 153-157

[127] Z V Marinkovi, L Mani, R Mari and O Miloevi, J.Eur. Ceram. Soc. 21 (2001) 2051-2055

[128] S Wang, W Wang, W Wang, Z Jiao, J Liu and Y Qian, Sensors & Actuators B: Chemical 69 (2000) 22-27

[129] S Y Wang, W Wang and Y Qian, Thin Solid Films 372 (2000) 50-53

[130] S Y Wang, W Wang and Y Qian, Mat. Res. Bull. 35 (2000) 2057-2062

[131] P S Patil, P R Patil and E A Ennaoui, Thin Solid Films 370 (2000) 38-44

[132] S Y Wang, Z P Qiao, W Wang and Y Qian, J. Alloys & Compounds 305 (2000) 121-124

[133] M C Baykul and A Balcioglu, Microelectronic Eng. 51-52 (2000) 703-713

[134] P R Patil and P S Patil, Mat. Res. Bull. 35 (2000) 865-874

[135] Y C Kang, I W Lenggoro, S B Park and K Okuyama, Mat. Res. Bulletin, 35, (2000) 789-798

[136] Y C Kang and S B Park, Mat. Letts. 40 (1999) 129-133

[137] Y Matsuzaki, M Hishinuma and I Yasuda, Thin Solid Films 340 (1999) 72-76

[138] A Ortiz, J C Alonso, V Pankov and D Albarran, J. Luminescence 81 (1999) 45-51

[139] V Jokanovic, Dj Janackovic, P Spasic and D Uskokovic, Nanostructured Mat. 12, (1999) 349-352

[140] E Djurado and M Labeau, J.Eur. Ceram. Soc. 18 (1998) 1397-1404

[141] S B Park, Y C Kang, I W Lenggoro and K Okuyama, J. Aerosol Sc., 29, (1998)S909-S910

[142] F L Yuan, C H Chen, E M Kelder and J. Schoonman, Solid State Ionics, 109 (1998) 119-123

[143] H K Singh and O N Srivastava, Phys. Letts. A, 240, (1998), 253-256

[144] Z V Saponjic, Z Rakocevic, N M Dimitrijevic, J M Nedeljkovic, V Jokanovic and D P Uskokovic, Nanostructured Mat. 10 (1998) 333-339

[145] Dj Janackovic, V Jokanovic, Lj Kostic-Gvozdenovic and D Uskokovic, Nanostructured Mat., 10, (1998) 341-348

[146] C H Chen, F L Yuan and J Schoonman, Eur. J. Solid State and Inorganic Chem. 35 (1998) 189-196

[147] R Abraham, F Guenard, K Lebbou, S Trosset, M T Cohen-Adad, J L Jorda and M Couach, Mat. Res. Bull. 33 (1998) 253-260

[148] Y R Roh, Y J Lee, H B Kim, H M Cho and S Baik, Sensors & Actuators A: Physical 64 (1998) 173-178

[149] P S Patil, E A Ennaoui, C D Lokhande, M Mller, M Giersig, K Diesner and H Tributsch, Thin Solid Films 310 (1997) 57-62

[150] P Fortunato, A Reller and H R Oswald, Solid State Ionics, 101-103, (1997) 85-89

[151] S Y Cho, I T Kim, D Y Kim, B K Kim, J H Lee and S J Park, Mat. Letts. 32 (1997) 271-273

[152] Y Harima, K Matsumoto, Y D Wang and K Yamashita, Thin Solid Films, 301, (1997) 95-104

[153] J M Nedeljkovi, Z V Aponji, Z Rakoevi, V Jokanovi and D P Uskokovi, Nanostructured Mat., 9, (1997) 125-128

[154] O Stryckmans, T Segato and P H Duvigneaud, Thin Solid Films, 283, (1996) 17-25

[155] S Stopic et al, (Serbian Academy of Sciences and Arts, Belgrade, Yugoslavia). Int. J. Powder Metall., 32, (1996) 59-65 Metal Powder Report 51(9)(1996) 34

[156] Y C Kang, S B Park and S W Kwon, J. Colloid & Interface Sci., 182, (1996) 59-62

[157] T Suzuki, K Itatani, M Aizawa, F S Howell and A K, J. Eur. Ceram. Soc. 16 (1996) 1171-1178

[158] S Stopi, I Iii and D Uskokovi, Mat. Letts. 24 (1995) 369-376

[159] C K Yun, B Park, S Whan, K Yun, Nanostructured Mat. 5 (1995) 777-791

[160] O Miloevi, B Jordovi and D Uskokovi, Mat. Letts. 19 (1994) 165-170

[161] S P S Arya and H E Hintermann, Thin Solid Films, 193-194 (1990) 841-846

[162] S P S Arya and H E Hintermann, J Less Common Metals, 164-165, (1990) 478-485

[163] N H Hur, W K Oh, Y K Park, Y S Moon and J C Park, Solid State Communications 76 (1990) 149-151

[164] O Sakurai, N Mizutani and M Kato, Int. J. High Techno. Ceram. 3 (1987) 175-176

[165] N Herlin, X Armand, E Musset, H Martinengo, M Luce and M Cauchetier, J. Eur.Ceram.Soc 16 (1996) 1063-1073.

[166] A Bouzidi, N Benramdane, A Nakrela, C Mathieu, B Khelifa, R Desfeux, A Da Costa, Mat. Sc.& Eng. B95 (2002) 141- 147.

[167] A Muller, N Herlin-Boime, F Tenegal, X Armand, J. Eur. Ceram. Soc., 23 (2003) 37-46.

[168] R Alexandrescu f Dumitrache, Nanotechnology 15 (2004) 537-545

[169] R Mueller, L Madler, S E Pratsinis, Chem. Eng. Sc. 58 (2003) 1969-1976.

Appendix 1

Some terminologies used in image analysis software- Image Tool^{TM}

In this appendix, definition of terms used in image analysis using the software package, Image Tool^{TM}, is done. In some cases, these terms carry very different meaning from the usual. *Area (σ_A)*: The area of the object, measured as the number of pixels in the polygon.

This measurement tends to produce a slight over-estimate of the object's area. If spatial measurements have been calibrated for the image, then the measurement will be in the units of that calibration; otherwise, it will be in square pixels. *Perimeter (P_R)*: The length of the outside boundary of the object, again taking the spatial calibration into account. The method used will tend to over-estimate the perimeter for convex objects. *Roundness: (R_n)*: Computed as:

$$R_n = \frac{4\pi\sigma_A}{P_R^2} \tag{5.2}$$

The result gives a value between 0 and 1. The greater the value, the rounder the object. If the ratio is equal to 1, the object is a perfect circle, as the ratio decreases from 1, the object departs from a circular form. *Elongation(ϵ_L)*: The ratio of the length of the major axis to the length of the minor axis.

$$\epsilon_L = \frac{\lambda_M}{\lambda_m} \tag{5.3}$$

The result is a value between 0 and 1. If the elongation is 1, the object is roughly circular or square. As the ratio decreases from 1, the object becomes more elongated (taken from

Baxes, Gregory, Digital Image Processing, 1994, p. 157). *Feret Diameter (d_f)*: The diameter of a circle having the same area as the object, it is computed as:

$$d_f = \frac{4\sigma_A}{\pi} \tag{5.4}$$

this provides a measure of the object's circle-ness. Basically the ratio of the feret diameter to the object's length will range between 0 and 1. At 1, the object is roughly circular. As the ratio decreases from 1, the object becomes less circular. *Compactness (C_t)*: This provides a measure of the object's circle-ness. Basically the ratio of the feret diameter to the object's length, it will range between 0 and 1. At 1, the object is roughly circular. As the ratio decreases from 1, the object becomes less circular. *Major Axis Length (λ_M)*: The length of the longest line that can be drawn through the object. The result will be in the units of the image's spatial calibration. *Major Axis Angle (θ_M)*: The angle between the horizontal axis and the major axis, in degrees. Minor Axis Length (λ_m): The length of the longest line that can be drawn though the object perpendicular to the major axis, in the units of the image's spatial calibration. *Minor Axis Angle (θ_m)*: The angle between the horizontal axis and the minor axis, in degrees. *Centroid*: The center point (center of mass) of the object. It is computed as the average of the x and y coordinates of all of the pixels in the object. *Gray Centroid*: Also called the brightness-weighted center of mass, this is the point in the object having equal brightness levels above, below, and to both sides of the point. It is computed as a weighted average of the x and y coordinates and the pixel brightness for all pixels in the object. If the image has been density calibrated, then the pixel brightnesses will be in these units. *Integrated Density*: Computed as the product of the mean gray level and the number of pixels in the image. If the image has been density calibrated, then the mean gray level will be in these units. *Min/Mean/Median/Mode/Max Gray Level, Std. Dev.*: Computes the given statistic for the pixels in the object, taking density calibration into account. *Measurement Precision*: The number of decimal places that should be used in the measurements sent to the results window.

Appendix 2

The linear chain model for derivation of dispersion relations in crystals

The purpose of this appendix is to serve as a reminder of the derivation of the phonon dispersion relations in materials. First it is convenient to begin with a simple monoatomic lattice of atoms arrange in an infinity linear chain as illustrated in Figure 5.1

When a chain of atoms with spacing a in a state of equilibrium are subject to an external force, they are displaced each of them with its own displacement. The n^{th} has an original equilibrium position of

$$x_n^0 = na \tag{5.5}$$

However after displacement, its new position becomes

$$x_n^0 = na + u_n \tag{5.6}$$

where u_n is the displacement of the n^{th} atom. The same analysis can be done for other atoms through out the lattice.

On the n^{th} atom, the force to the right is given as

$$F_R = k\left(u_{n+1} - u_n\right) \tag{5.7}$$

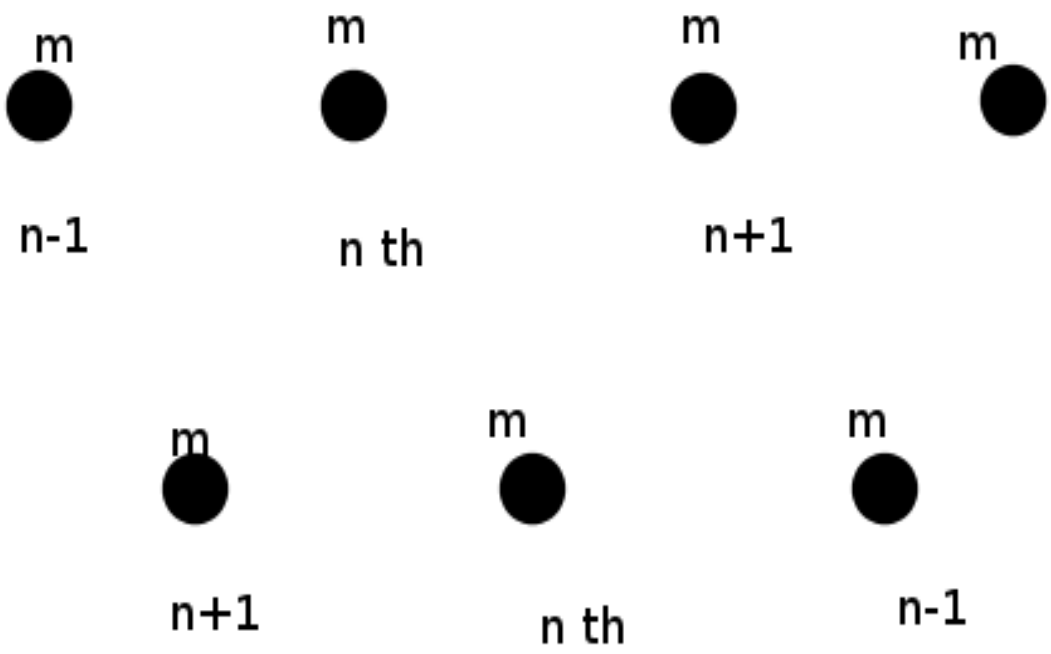

Figure 5.1: A simple monoatomic lattice with the above chain depicting atoms in equilibrium and the chain below represents the same chain under a displacement due to an external force

and similarly the force to its left is

$$F_L = -k\left(u_{n-1} - u_n\right) \tag{5.8}$$

where the negative sign in the Equation 5.8 only signifies the sign convention that if left is negative then right is positive

The net force is force is a sum of the two force which gives

$$m\frac{d^2u_n}{dt^2} = -k_F\left(u_{n+1} - 2u_n + u_{n-1}\right) \tag{5.9}$$

where k_F is the force constant of the material bonds.

When a trial solution is substituted into the differntial equation 5.9 a dispersion relation of the following form is obtained:

$$\omega = \sqrt{\frac{4k_F}{m}} sin\left(\frac{aq}{2}\right) \tag{5.10}$$

This equation is true for a monoatomic lattice. However for a diatomic lattice, it can be shown that two simultaneous differential equation are obtained and summarized here as

$$\begin{aligned} m_1 \tfrac{d^2 u_n}{dt^2} &= C\left(\nu_{n+1} - 2u_n + \nu_{n-1}\right), \\ m_2 \tfrac{d^2 u_n}{dt^2} &= C\left(n_{n+1} - u_n + 2\nu_n\right) \end{aligned} \tag{5.11}$$

Upon proper substitution these simultaneous equation can solve use the determinant which equal to zero given below

$$\begin{aligned} &\mid 2C - m_1\omega \qquad\quad - C\left(1 + exp(-iKq)\right) \mid u \mid, \\ &\mid -C\left(1 + exp(-iKq)\right) \qquad 2C - m_2\omega) \mid \nu \mid \end{aligned} \tag{5.12}$$

This analysis yields the following equation

$$\begin{aligned} &m_1 m_2 - 2\left(m_1 + m_2\right) C\omega^2 + 2C^2\left(1 - cos(aq)\right) = 0, \\ &\omega_1^2 = \tfrac{Cq^2a^2}{2m_1m_2}, && optical maximum \\ &\omega_2^2 = 2C\left(\tfrac{1}{m_1} + \tfrac{1}{m_2}\right), && acoustic maximum \end{aligned} \tag{5.13}$$

The fact the cosine term in the round brackets can be converted to sine by trigonometric identities which in turn can be expanded using MacLaurin or Taylor series, enables one to see that the phonon dispersion relation can be approximated by neglecting the higher terms to the following expression

$$\omega\left(q\right) = A \pm Bsin^2(q) \sim A \pm Bq^2 \tag{5.14}$$

as assumed in the main text of this dissertation.

Appendix 3

Scanning electron micrographs of some WO_3 samples and the size distribution of their grains by Image Tool^{TM} software

This appendix attempts to present a gallery of some of the scanning electron micrographs of the tungsten trioxide samples. The images show how the morphology of WO_3 surface and its grains evolve as the temperature of material deposition is increased. Each SEM micrograph has a size distribution histogram in micrometers juxtaposed to it. The data obtained were used to relate size to temperature of deposition as presented in the main text.

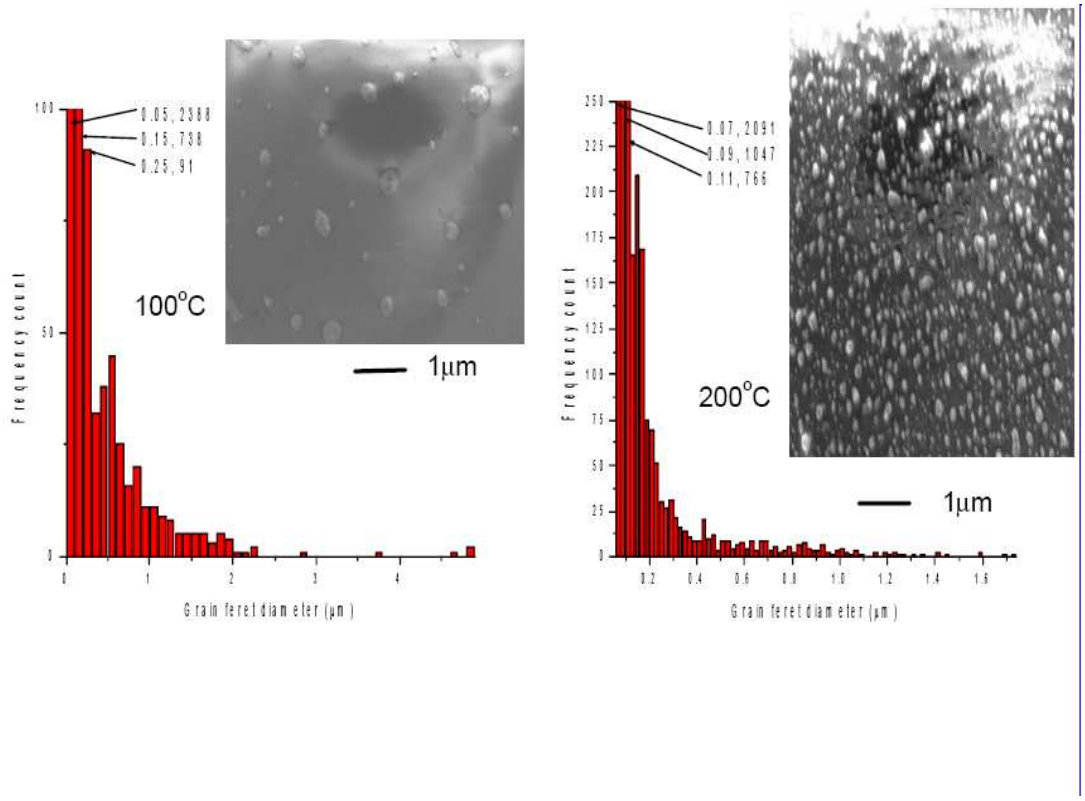
0.05, 2388
0.15, 738
0.25, 91
100°C
1μm
Frequency count
Grain feret diameter (μm)
0.07, 2091
0.09, 1047
0.11, 766
200°C
1μm
Frequency count
Grain feret diameter (μm)

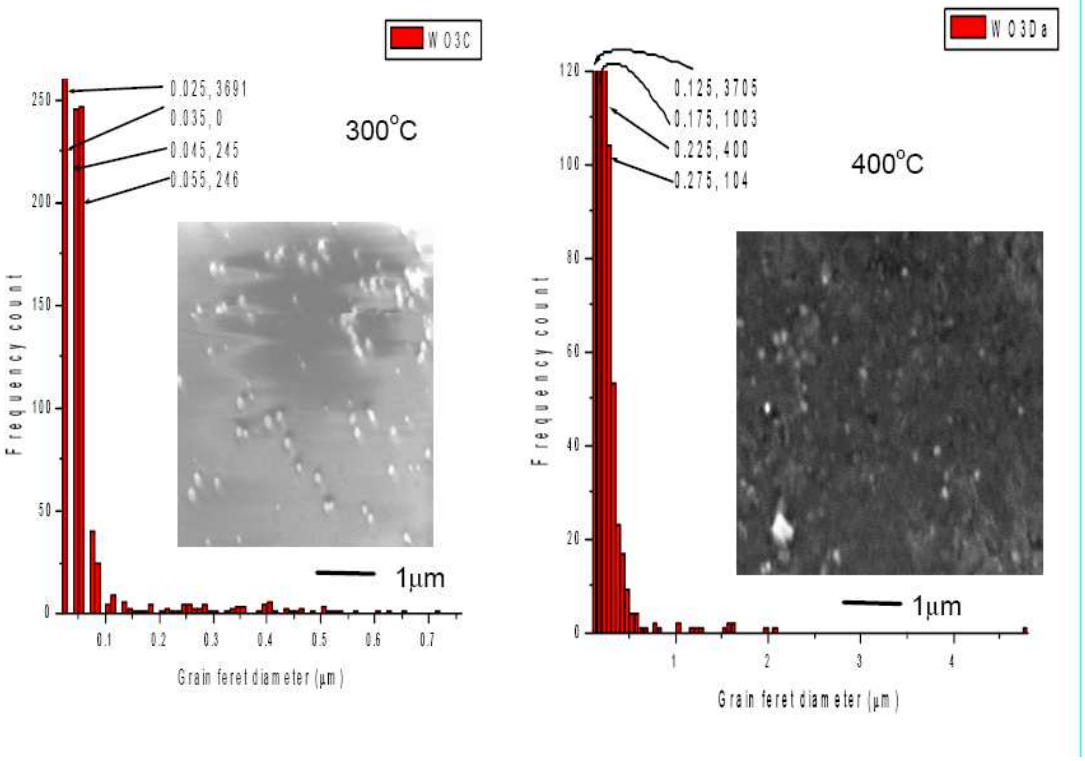
WO3C
0.025, 3691
0.035, 0
0.045, 245
0.055, 246
300°C
1μm
Frequency count
Grain feret diameter (μm)
WO3Da
0.125, 3705
0.175, 1003
0.225, 400
0.275, 104
400°C
1μm
Frequency count
Grain feret diameter (μm)

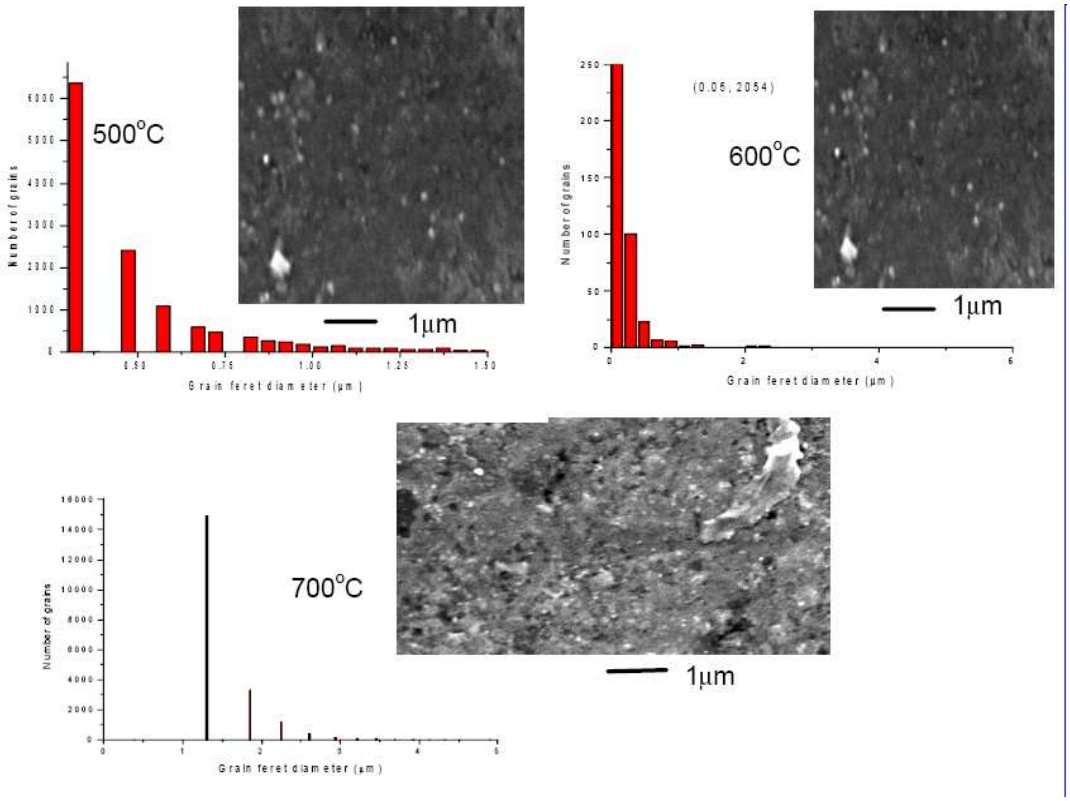
500°C
1μm
Number of grains
Grain feret diameter (μm)
(0.05, 2054)
600°C
1μm
Number of grains
Grain feret diameter (μm)
700°C
1μm
Number of grains
Grain feret diameter (μm)